

We are IntechOpen, the world's leading publisher of Open Access books Built by scientists, for scientists

4,800

Open access books available

122,000

International authors and editors

135M

Downloads

Our authors are among the

154

Countries delivered to

TOP 1%

most cited scientists

12.2%

Contributors from top 500 universities



WEB OF SCIENCE™

Selection of our books indexed in the Book Citation Index
in Web of Science™ Core Collection (BKCI)

Interested in publishing with us?
Contact book.department@intechopen.com

Numbers displayed above are based on latest data collected.

For more information visit www.intechopen.com



Digital Micro PIV (μ PIV) and Velocity Profiles *In Vitro* and *In Vivo*

Aristotle G. Koutsiaris

*Bioinformatics Lab, School of Health Sciences,
Technological Educational Institute (TEI) of Larissa, Larissa,
Greece*

1. Introduction

The term **Particle Image Velocimetry (PIV)**, in the technical world, is used to describe a powerful, automated flow visualization method which quantifies the instantaneous flow velocity field in 2 dimensions. PIV gives valuable information on how velocity field changes at a specific measurement plane, at regular time intervals, selected by the operator.

Correlation techniques were used extensively for the measurement of fluid velocity. In temporal correlation techniques, velocity is inversely proportional to the transit time for flow tracers to cross a fixed distance. In **spatial correlation techniques**, the velocity is directly proportional to the displacement of flow tracers in a fixed time interval. In this sense, many video techniques, high speed cinematography and PIV can be classified as spatial correlation techniques.

The term "**Digital**" refers to the fully digital implementation of the method, namely the use of a digital camera connected directly to a digital electronic computer in order to acquire flow images and then to estimate the correlation function. This may seem a common place today, but a lot of early implementations used to have special electrooptical and electromechanical hardware for the estimation of the correlation function (optical correlation) or film cameras with laser scanners (optical - digital correlation). Later, fully electronic PIV implementations appeared using analog together with digital hardware: analog CCD cameras connected to video recorders produced video tape images which were digitized by computers (Gardel et al., 2005). These implementations were limited by their analog components.

The term "**Micro**" refers to the length scale of the microfluidic environment ranging between $1\mu\text{m}$ and $1000\mu\text{m}$. The word "environment" is a general term for every possible microstructure inside which the fluid under study flows.

This chapter is a medium size review on **Digital micro PIV (μ PIV)** and its applications on the velocity profiles *in vitro* and *in vivo*. Parts of sections 6 and 7 come from a mini review paper (Koutsiaris, 2010b).

2. Components of a Digital μ PIV system

A complete PIV implementation is subdivided into four steps (Koutsiaris et al., 1999): 1) seeding of the flow, 2) illumination of the flow plane of interest with a light sheet, 3) image capture by a camera placed at right angles to the illuminated flow plane, and 4) data processing.

There are **three principal differences** between an ordinary macroscopic and a μ PIV system. **First**, as it was mentioned in the introduction, it is the **length scale** of the fluidic circuit under study (hence the name “micro”). **Second**, as a consequence of the first difference, it is the design of the optical system, which has as a minimum requirement some kind of a **microscope** objective lens. **Third**, the thickness of the measurement plane is defined by the optical system using **volume illumination** and not by the thickness of an illuminating light sheet. Forming a light sheet with a thickness between 1 and 20 μm and aligning it properly in the microfluidic circuit is very difficult.

In this section, the main components of a Digital μ PIV system are described: **1)** the microfluidic circuit with appropriate flow tracers, **2)** the optical system, **3)** the digital electronics system and **4)** the computer software. These components are presented in schematic form in figure 1.

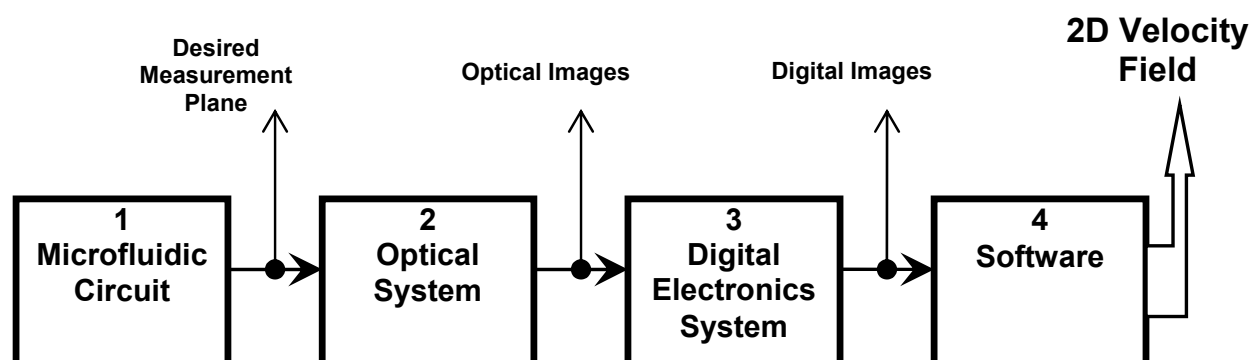


Fig. 1. The four main components of a Digital μ PIV system.

2.1 Microfluidic circuit and flow tracers

The usual implementation of the microfluidic system comprises some kind of a microstructure-microchannel (microduct, microtube, capillary) connected to a syringe pump (figure 2). The microchannel can be made of various materials such as glass (Koutsiaris et al., 1999; Meinhart et al., 1999), biocompatible polymers and collagen gel inside silicone elastomer (Chrobak et al., 2006; Potter & Damiano, 2008). Biocompatible polymers can be classified to thermoplastic polymers such as Poly Methyl MethAcrylate (PMMA, Timgren et al., 2008) and to elastomeric polymers such as Poly DiMethiSiloxane (PDMS, Lima et al., 2008).

A lot of research was directed during the past 10 years to **biocompatible polymers**, due to their advantages over glass. PDMS in particular is permeable to gases such as oxygen and there is no need to use a refractive index matching liquid. The ultimate tensile stress and Young's elastic modulus are much closer to those of blood vessels in comparison to glass and sealing does not require any complex bonding technique. In addition, various

microdevices such as micropumps can be integrated easily in a PDMS device. A more detailed discussion on PDMS advantages can be found in the paper of Lima et al. (2008).

The microfluidic system can be a part of a MicroElectroMechanical Systems (MEMS) device. Other typical microdevices are microheat sinks, micropumps, microturbines, microengines, micromixers and microsensors. More details on the design, fabrication and applications of MEMS devices can be found in review papers (Hassan, 2006) and in books edited by Gad-el-Hak (2005) and Breuer (2005) and written by Nguyen and Wereley (2002).

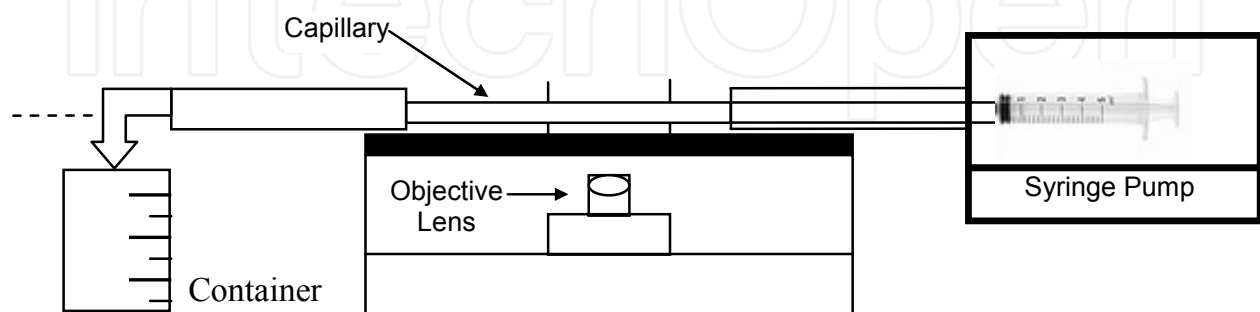


Fig. 2. A typical microfluidic circuit with a syringe pump, on an inverted microscope.

When the experimental conditions are right, the syringe pump is not needed since the necessary driving force can be controlled with the height difference (DH, figure 3). In this way a more economic set up is possible.

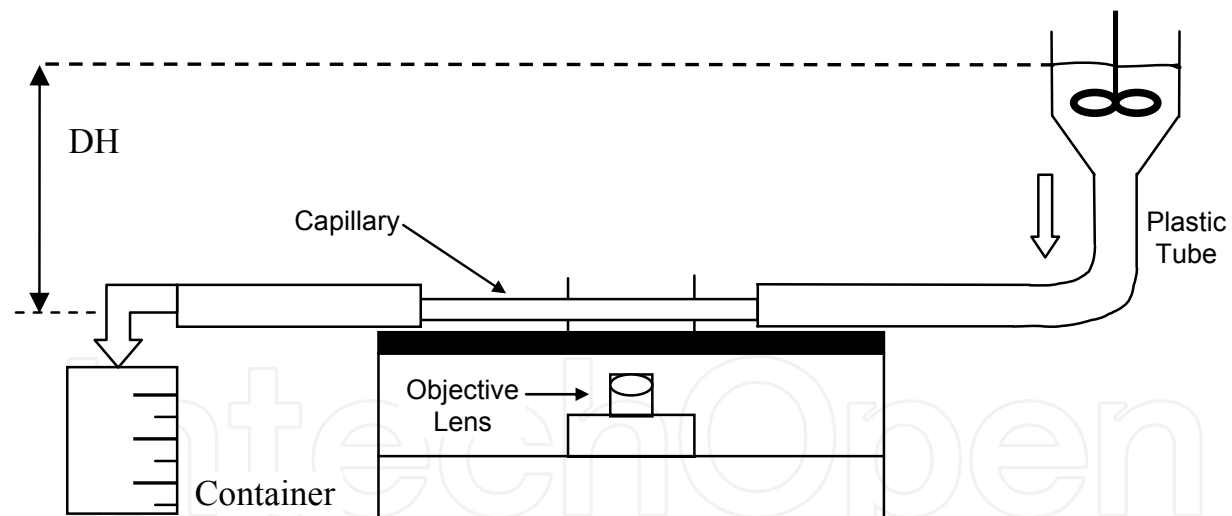


Fig. 3. A microfluidic circuit without any syringe pump (Koutsiaris et al., 1999). The driving force is provided by the height difference DH.

The basic characteristic of a successful flow tracer is that it should accurately follow the flow with an appropriate specific gravity matching (Stokes equation, Raffel et al., 2007). Flow tracers are usually made of fluorescent PolyStyrene Latex (PSL) particles but the final choice depends on the fluid. When the particle diameter is less than $\approx 0.5 \mu\text{m}$ and characteristic velocities are less than $\approx 1\text{mm/s}$, the Brownian motion should be taken into account (Wereley and Meinhart 2010). More details on Brownian motion and the Saffman effect can be found in the textbook edited by Breuer (2005).

In addition, the particle diameter distribution should be monodispersive (diameter values distributed over a very limited range around the mean value). We shall see later that this makes easier the design and error evaluation.

2.2 Optical system

2.2.1 Basics

The basic optical characteristics carved on the metallic surface of every microscope objective lens are magnification (M) and **numerical aperture (NA)**. In simple terms, M shows how many times the perpendicular to the optical axis dimension of an object lying in the object plane is enlarged in the image plane on the other side of the lens. A schematic diagram of these planes is shown in figure 4.

Magnification is a characteristic easily perceived by the majority of people who often seem to neglect the second equally important optical characteristic of a microscope objective lens, the NA:

$$NA = \eta \sin\Theta \quad (1)$$

Where η is the refraction index of the material between the lens and the specimen and Θ is the half angle of the cone of light received by the objective lens (figure 4). It should be noted that η is by definition always greater or equal to 1 and is a function of the light wavelength λ ($\eta = f(\lambda)$).

The NA is a very important lens specification for μ PIV applications because of the following reasons: **First**, it determines in a non-linear way the light gathering ability of the objective lens: the higher the NA the much higher the light gathering capacity. **Second**, it specifies, in an inversely proportional way, the resolving ability (RA) or simply “resolution” of the objective lens, i.e. the smallest discernible distance between two objects (points) in the object plane:

$$RA = 0.61 \lambda_a / NA \quad (2)$$

The above formula was derived using the Rayleigh criterion and assuming paraxial conditions (optical rays close to the optical axis). λ_a is the wavelength of light in the air.

Third, the NA specifies in a non-linear way, the depth of field or depth of focus DoF (figure 4) of an objective lens: the higher the NA the much lower the DoF. A typical “simple” equation quantifying the DoF of an objective lens was proposed by Shillaber (1944, as cited in Delly, 1988):

$$DoF = \lambda_a \frac{\sqrt{\eta^2 - NA^2}}{NA^2} \quad (3)$$

However, there seems to be a difference between the DoF seen by an observer through an eyepiece and the DoF_v when a video camera is attached on the microscope (Nakano et al., 2005):

$$DoF_v = \frac{\lambda_a \cdot \eta}{NA^2} + \frac{\eta \cdot px}{M \cdot NA} \quad (4)$$

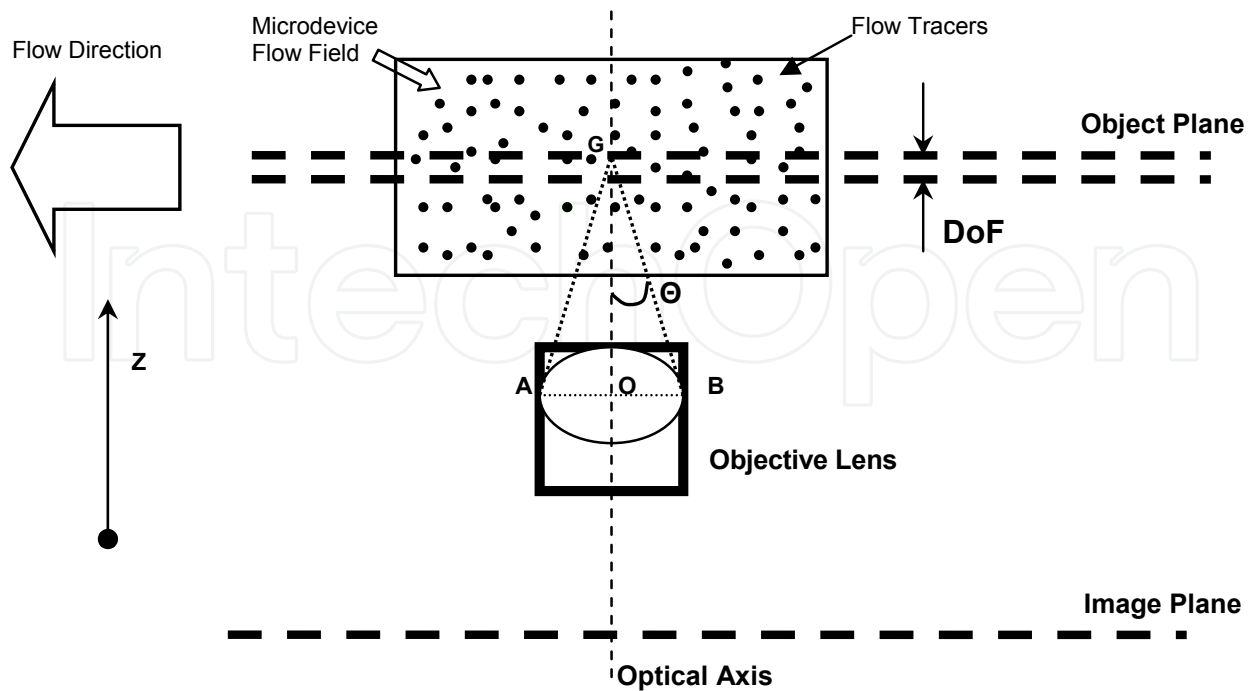


Fig. 4. The object and image planes of a microscope objective lens have a finite depth along the optical axis. The object plane depth is called **Depth of Focus (DoF)**. Θ is the half cone angle of the objective light rays focused on a **focal point G** inside the object plane. OG is the focal distance of the objective lens and AB is its diameter D .

Where p_x is the pixel size of the video camera. The difference in the DoF estimations given by the 2 formulas becomes important for $NA > 0.5$, as it is shown in Table 1.

Objective Lens (M/NA)	DoF (Shillaber) (μm)	DoF _v (Video) (μm)	Relative Difference $\frac{\text{DoF} - \text{DoF}_v}{\text{DoF}_v}$ (%)
10/0.25	8.5	9.3	- 9
20/0.5	1.9	2.3	- 17
40/0.6	1.2	1.6	- 25
40/0.75	0.6	1	- 35
60/1.4	Not defined	0.3	-

Table 1. The Depth of Field (DoF) and the video Depth of Field (DoF_v) depend on the objective lens. Numbers were estimated assuming: $\lambda_a = 0.55 \mu\text{m}$, $\eta = 1$, pixel size $p_x = 16 \mu\text{m}$.

Another optical characteristic of the microscope objective lens, used frequently in photographic cameras, is called *f* number (*f*#). The *f*# is closely related to the NA, but is defined in purely geometrical terms:

$$f\# = \frac{OG}{D} \quad (5)$$

Where OG is the focal distance of the objective lens and D is its diameter (figure 4). The mathematical relationship between NA and $f\#$ can be derived from equations 1 and 5:

$$f\# = \frac{1}{2} \sqrt{\left(\frac{\eta}{NA}\right)^2 - 1} \quad (6)$$

This is a strong non linear relationship which can be significantly simplified assuming paraxial conditions ($\tan\Theta \approx \sin\Theta \approx \Theta$, Bown et al., 2005):

$$f\#_P = \frac{\eta}{2NA} \quad (7)$$

The assumption of paraxial conditions in equation 7, leads to a relative error less than 12% when $f\# > 1$ or $(NA/\eta) < 0.45$.

2.2.2 Measurement Plane Width (MPW)

In classical PIV the measurement plane width (MPW) is defined by a laser light sheet because outside particles do not influence the result. However in μ PIV, there is not any laser light sheet and most of the flow field is illuminated in a situation commonly referred to as “**volume illumination**” (figure 5). This means that an unknown amount of particles below and above the level of the object plane contributes to the position of the maximum of the correlation function and consequently to the velocity result (see Section 2.4). These particles are shown in the areas between the 2 solid lines and the 2 dashed lines of figure 5. The position of the 2 solid lines, depending on many factors related to the experimental set up (but primarily on the objective lens NA), can not be located accurately and therefore the MPW can not be determined in a rigorous way.

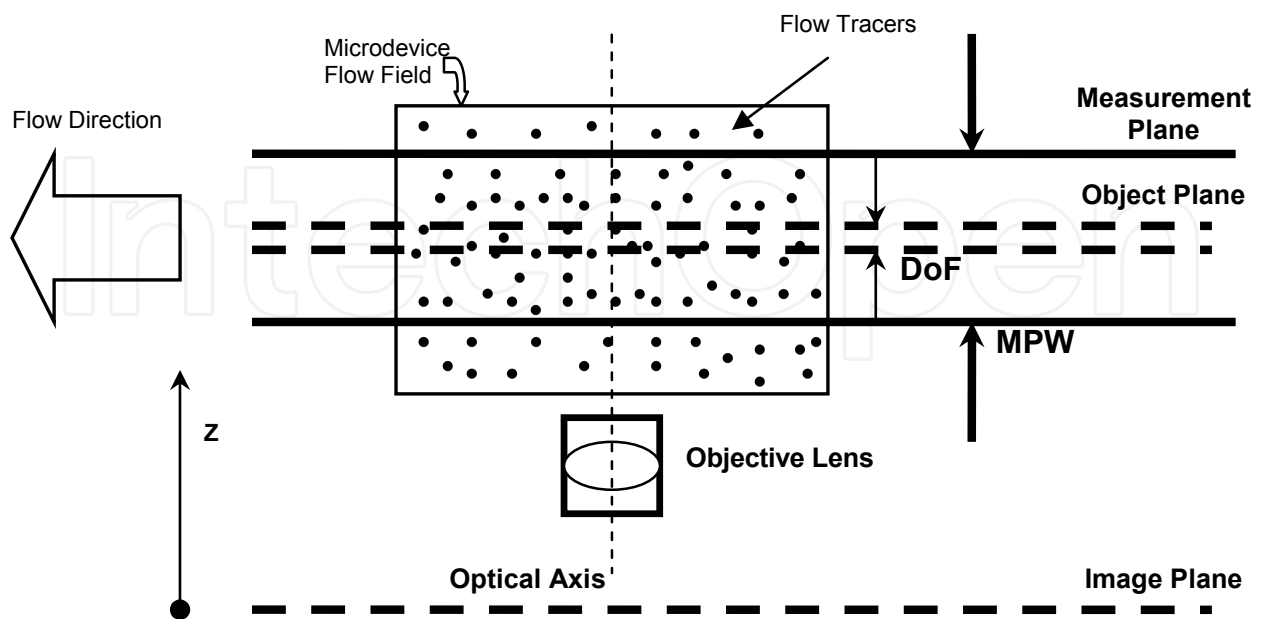


Fig. 5. The μ PIV volume illumination principle: the depth of focus (DoF) is always much lower than the measurement plane width (MPW).

In an attempt to quantify the contribution of out of focus particles in the velocity result, Olsen & Adrian (2000) introduced the concept of the “correlation depth”. The correlation depth (Z_{cor}) was defined as the axial distance from the object plane in which a particle becomes sufficiently out of focus so that it no longer contributes significantly to the velocity estimation (Werely & Meinhart, 2005). The **measurement plane width MPW** (proposed by Werely et al., (2000), as cited in Olsen & Adrian, (2000)) can be defined as double the Z_{cor} :

$$MPW = 2 \cdot Z_{cor} = 2 \cdot \sqrt{\frac{1 - \sqrt{\epsilon}}{\sqrt{\epsilon}} \left[f\#_p^2 d_p^2 + 5.95 \frac{(M+1)^2 \lambda_a^2 f\#_p^4}{16 \cdot M^2} \right]} \quad (8)$$

Where ϵ is the relative contribution of a particle located at a distance Z_{cor} from the object plane, $f\#_p$ is the f number with paraxial approximation (equation 7), d_p is the particle diameter in the object plane, M is the objective lens magnification and λ_a is the wavelength of light in the air. According to Werely & Meinhart (2010), equation 8 agrees more closely to experiments than when using the exact f number relationship (equation 6).

A series of MPW values for various objective lenses and for a $d_p = 1\mu\text{m}$ are shown in Table 2 ($\epsilon = 0.01$, $\lambda_a = 0.55\mu\text{m}$, $\eta = 1$, $p_x = 16\mu\text{m}$). The relative difference between the MPW and the DoF_V is **higher than 300%** for all kinds of objective lenses.

Objective Lens (M/NA)	DoF_V (Video) (μm)	f_p	MPW (μm)	Relative Difference $\frac{MPW - DoF_V}{DoF_V}$ (%)
10/0.25	9.3	2	37.4	302
20/0.50	2.3	1	10.4	352
40/0.60	1.6	0.83	7.5	367
40/0.75	1	0.66	5.35	435
60/1.4	0.3	0.36	2.40	700

Table 2. Video Depth of Field (DoF_V) in comparison to the Measurement Plane Width (MPW).

In order to see the effect of the particle diameter d_p on the MPW given by equation 8, the reader can see table 1 in Bourdon et al. (2004) and in Werely & Meinhart (2010), even though there seems to exist a discrepancy in the values given by the 2 groups (in addition, Werely & Meinhart (2010) do not mention the light wavelength used in their calculations). For the effect of d_p on MPW using the exact definition of f number, the reader can see table 2.2 in Werely & Meinhart (2005) where it is shown that, for “dry” lenses, there is not a significant effect of particle diameter on MPW when $d_p < 0.5\mu\text{m}$.

2.2.3 Effective Diameter (d_E)

The recorded image of a tracer particle is the convolution result between the geometric image of the particle and the point response function of the imaging system, given diffraction limited optics. The diameter of the geometric image of a particle is Md_p . The particle diameter d_p needed for determining the geometric image dimension is usually measured using an optical microscope and an object micrometer (micrometric ruler). For particle diameters less than about $0.2\mu\text{m}$ other techniques must be used such as atomic force microscopy and electron microscopy.

The diameter of the point response function d_s is given by the Airy function:

$$d_s = 2.44 (M+1) f\# \lambda_a \quad (9)$$

Adrian and Yao (1985, as cited in Werely & Meinhart, 2005) found that the Airy function can be approximated accurately by a Gaussian function. Given spherical particles and diffraction limited optics the geometric image can also be approximated accurately by a Gaussian function and the total diameter d_E (effective diameter in microns) of the particle in the image plane can be approximated by:

$$d_E = \sqrt{(Md_p)^2 + d_s^2} \quad (10)$$

Then effective diameter can be converted to pixels by using the pixel size of the video camera. The contribution of the geometric and the point response components in the final d_E is shown in Table 3 for various particle diameters, in the case of a 10/0.25 objective lens ($\lambda_a = 0.55 \mu\text{m}$).

Particle Diameter d_p (μm)	Geometric Component $M d_p$ (μm)	Point Response Component d_s (μm)	Effective Diameter d_E (μm)	Relative Difference $\frac{d_s - d_E}{d_E}$ (%)
0.1	1	28.6	28.6	0
0.5	5		29.0	- 1.4
0.7	7		29.4	- 2.7
1.0	10		30.3	- 5.6
3.0	30		41.4	- 31.0
5.0	50		57.6	- 50.3

Table 3. The geometric and the point response component of the effective particle diameter d_E .

As it can be observed in the gray line of table 3, when the geometric component is **less than one third of d_s** , then it contributes by less than 5% in the final effective diameter d_E . In practice this means that for an objective lens 10/0.25, all particles with diameters $d_p < 1 \mu\text{m}$ will have an effective diameter approximately equal to d_s .

In Table 4, the point response diameter d_s is given for commonly used objective lenses and $\lambda_a = 0.55 \mu\text{m}$. It should be noted that in the case of oil immersion objectives (60/1.4) the NA is equal to the refraction index of the medium and using equation 6 this gives $f\# = 0$ (hence $d_s = 0$, which is not true). In this case, the $f\#$ should be estimated by its original definition (equation 5). In Table 4, for the case 60/1.4 it was assumed that $f\# = 0.2$.

Objective Lens (M/NA)	10/0.25	20/0.50	40/0.60	40/0.75	60/1.4
F#	1.94	0.87	0.66	0.44	0.2
d_s (μm)	28.6	24.5	36.3	24.2	16.4

Table 4. Point response diameter d_s for various objective lenses.

The effective diameter d_E is very important because it contributes to the random and bias error components (Section 3) in the displacement and velocity estimation. It has been shown (Prasad et al., 1992) that, when the centroiding technique is chosen for locating the autocorrelation peak, the total displacement error is minimized by selecting $d_E \approx 2$ pixels. The same result was obtained when a Gaussian peak fit estimator was used (Westerweel 1997). Since the pixel size is usually fixed, depending on the CCD camera, the number of pixels corresponding to the effective diameter d_E can be arranged by selecting the appropriate optics and flow tracers. It should be noted however, that later authors preferred a design of $d_E \approx 4$ pixels (Buffone et al., 2005; Koutsiaris et al., 1999; Meinhart et al., 1999).

Finally, it should be noted that d_E depends also on the vertical distance in the z direction from the object plane (figure 5). So, for out of focus particles located outside the object plane, there is a z dependent third term added in equation 10. This is beyond the scope of this chapter (see Bown et al., 2005).

2.2.4 Fluorescence μ PIV

Volume illumination can be implemented with 2 different experimental set ups: **fluorescence** and **brightfield** illumination. In the experimental set ups with fluorescence, **darkfield images** are produced by the camera and are sent to the PC for off line processing (figure 6). In a darkfield image the tracers appear bright in a dark background, as in the

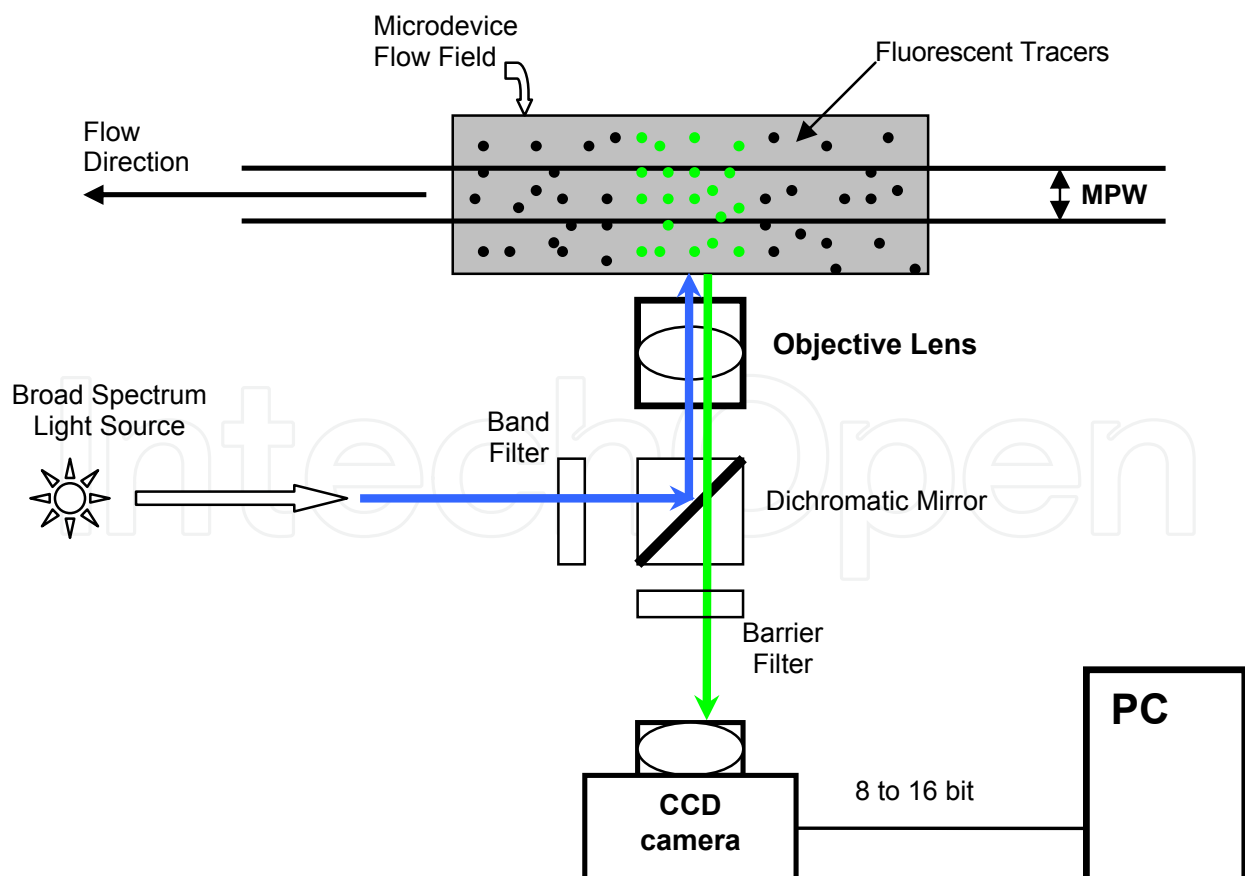


Fig. 6. Digital μ PIV set up with fluorescence. MPW: Measurement Plane Width.

classical film negatives. When a monochromatic light source (laser) is used, the band pass filter is not necessary.

The first μ PIV system using an upright **epi-fluorescent** microscope was reported by Santiago et al. (1998). The vast majority of fluorescent microscopes are epi-fluorescent (figure 6), meaning that image sensors detect the back scattered (reflected) fluorescence from the object plane and not the transmitted fluorescence. Santiago et al. (1998) used 300 nm in diameter, fluorescently labeled, PSL particles in the flow field between a microscope slide and a 170 μ m thick coverslip. The liquid thickness between the slide and the coverslip was $\approx 5 \mu$ m and the spatial resolution was $6.9 \times 6.9 \times 1.5 \mu$ m. Because of the large time delay between successive images, they managed to measure only low velocities of the order of 35 μ m/s. One year later, Meinhart et al. (1999), using an inverted epi-fluorescent microscope, and a different digital camera illuminated by 2 Nd:YAG lasers, reduced the time delay between images by more than a factor of 100 and managed to measure velocities of the order of 10 mm/s.

2.2.5 Brightfield μ PIV

In brightfield μ PIV images, the tracers appear dark in a **bright background**, as the objects in the positive photos of everyday photographic albums. This happens because particles are not fluorescent and instead of emitting they actually absorb light.

The first μ PIV system without fluorescence, using an inverted brightfield microscope (transmission mode) was reported by Koutsiaris et al. (1999). The vast majority of the brightfield microscopes work in **transmission mode**, meaning that video cameras detect the transmitted (forward scattered) light from the object plane (figure 7).

Koutsiaris et al. (1999) used borosilicate glass particles with a mean diameter of 10 μ m to seed the flow of a suspension consisting of glycerol and water. The distinctive optical characteristic of this suspension was the similar refractive index with the glass capillary (figure 8). They demonstrated for the first time that μ PIV is possible in cylindrical microtubes (150 to 300 μ m internal diameter) by using the aforementioned suspension and by surrounding the capillary with a fluid having a similar refractive index with the capillary. The spatial resolution of their velocity fields was $26.2 \times 335 \times 10 \mu$ m, optimized for the velocity profile measurement inside the capillaries and velocities up to the order of 5 mm/s were measured. In addition, the application of the μ PIV technique at the microvessels of a living animal was proposed for the first time and a discussion on possible obstacles of such an attempt was presented.

A brightfield μ PIV set up can be considered as the dual counterpart of the fluorescence set up, but without requiring complex and expensive fluorescence hardware such as a special light source, filters and a dichromatic mirror. It seems that a brightfield set up has a higher in focus noise in comparison to a fluorescent set up but a smaller contribution to noise from out of focus particles. In addition, dark particles with diameters lower than about 0.5 μ m can not be easily resolved by an optical microscope. It seems that these topics as well as the MPW and the d_E in the case of a brightfield set up have not been fully exploited by the research community yet.

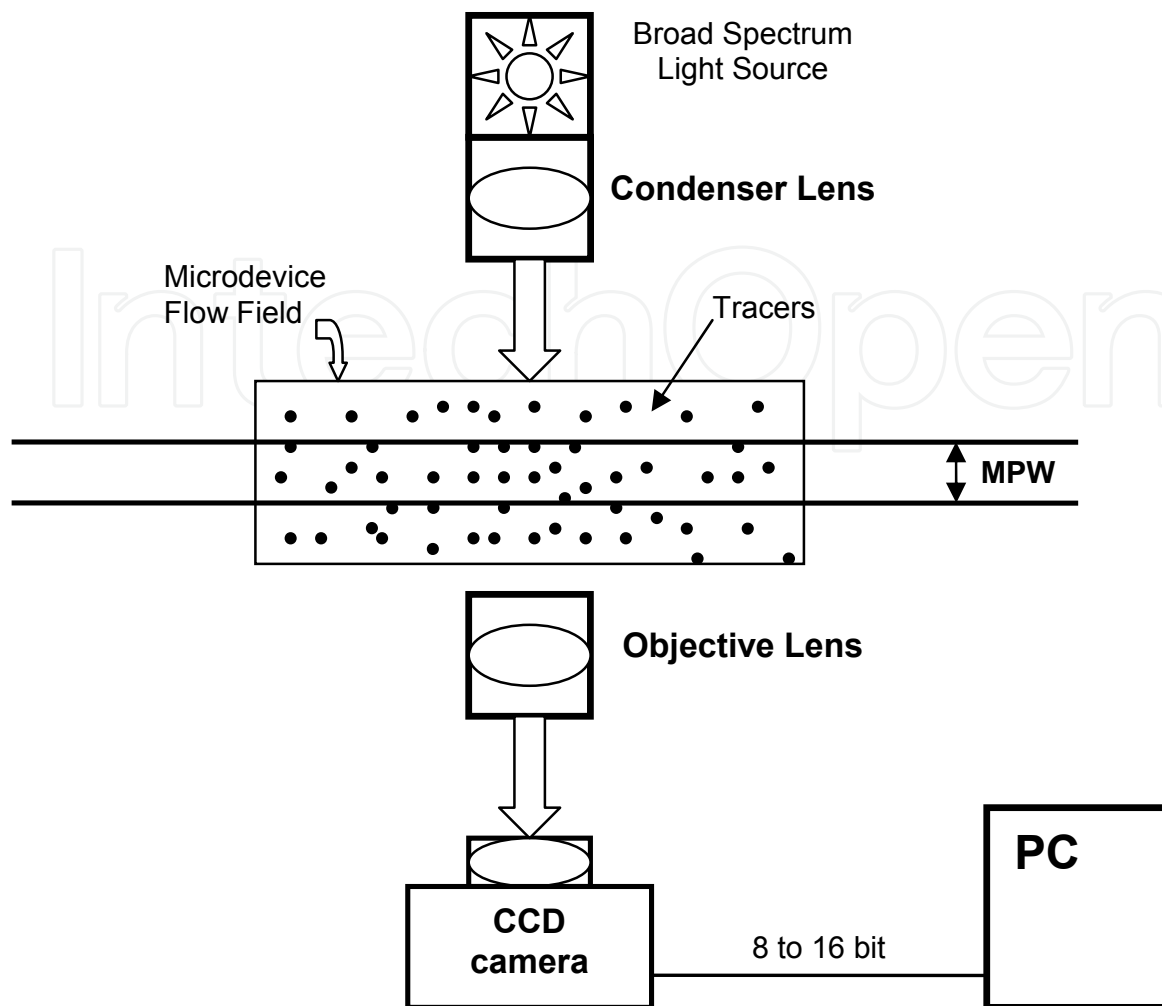


Fig. 7. Digital μ PIV set up with brightfield illumination. MPW: Measurement Plane Width.

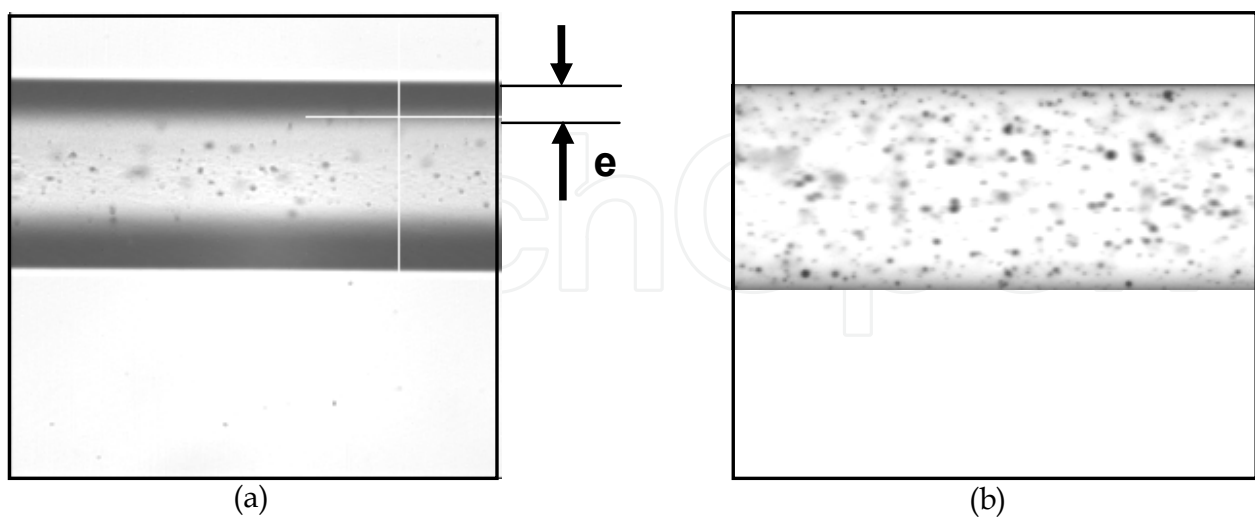


Fig. 8. Glass cylindrical capillaries with internal diameters of $\approx 275 \mu\text{m}$. (a) Glass particles suspended in water: in the diametric plane, approximately 41% of the internal diameter is not visible (black band $e \approx 57 \mu\text{m}$). (b) The black bands disappeared when the glass particles were suspended in a mixture of 75% glycerol and 25% water.

2.2.6 Confocal μ PIV

The incorporation of confocal imaging in a μ PIV experimental set up provides a powerful experimental tool introduced by Park et al. (2004). In a confocal optical system the object plane of interest is scanned point by point by a laser beam. Each scanned point of the measurement plane is the optical conjugate of a pinhole located in the image plane of the objective lens. This fact reduces the signal intensity passing through the pinhole, but also reduces dramatically the out of focus background light, producing a rigorously defined optical slice in the object plane with a thickness much smaller than that in ordinary optical systems.

The confocal μ PIV has the following advantages over the classical μ PIV: **first**, the difference between the depth of focus (DoF) and the measurement plane width (MPW) is significantly smaller due to the confocal superiority over classical optics in terms of axial resolution.

Second, the increased axial resolution implies sharp reduction of background light from out of focus images and higher signal to noise ratios for the correlation operation. **Third**, there are no different effective particle diameters produced from their different distances from the object plane.

Despite the numerous advantages of the confocal μ PIV, there are some disadvantages stemming out from the operating principle of confocal imaging according to which a single point can only be imaged at one instance in time. This means that each image is produced by scanning a 2D plane point by point, which implies restrictions in the frame rate and increased cost due to complex hardware. Restrictions in the frame rate (hence in the maximum measurable velocity) can be overcome by using a superfast Nipkow disk (Lima et al., 2006; Park et al., 2004). However, this action further increases complexity and cost.

It seems that, confocal μ PIV has not been applied without fluorescence. This would perhaps be feasible in relatively transparent media which do not attenuate light intensity significantly. In addition, image processing of confocal images could increase even more the image quality (signal to noise ratio).

Combining 2D velocity fields at different z positions (figure 5), confocal data can be used in steady flows to calculate the 3D velocity field by applying the continuity equation. Other methods for the quantification of the 3D velocity field are digital holography, stereo μ PIV and particle image defocusing. In stereo μ PIV (Bown et al., 2006; Lindken et al., 2006) all 3 velocity components in space can be extracted from a single 2D plane. More details on the 3D μ PIV techniques can be found in the review papers of Lee & Kim (2009) and Werely & Meinhart (2010) and a comparison between stereo μ PIV and the multiple 2D velocity field technique was presented in the paper of Bown et al. (2006).

2.3 Digital Electronics System (camera)

The digital electronics component of μ PIV set up comprises a digital video camera, a frame grabber and a personal computer. The usual way is to put emphasis on the camera design, but its performance depends heavily on the frame grabber design so, they usually come together.

Most digital cameras are based on the **CCD (Charge-Coupled Device)** technology. Briefly, photons from the optical image of the measurement plane hit on the surface of the camera producing free electrons, which in their turn are trapped inside potential wells. Each

potential well of the camera corresponds to a pixel. Therefore, the higher the light intensity on the camera sensor, the higher the amount of electrons trapped inside the potential wells, and the higher the gray value of the corresponding pixel. In fact it is the product of the light intensity and the exposure time which affects the final gray value of a pixel. The most important characteristics of a CCD camera are: **1)** the quality of the CCD sensor, **2)** the architecture of the CCD sensor, **3)** the sensitivity (lowest detectable light intensity), **4)** the frame rate capacity (frames per second, fps) and **5)** the gray level dynamic range where the camera operates linearly.

Monochrome CCD cameras are preferable to color CCD cameras (Breuer 2005), because colors usually increase the complexity and the cost of a camera at the expense of frame rate, sensitivity and dynamic range. In addition pixels should be square to avoid complexities related to the conversion from image domain (pixels) to real dimensions.

For μ PIV systems, non interlaced high speed digital cameras are preferred. A camera is of the “**high speed**” type, when it can acquire more than 25 (EUROPE) or 30 (USA and JAPAN) full frames per second (fps). But in special μ PIV applications, speeds up to 2000 fps may be necessary. A high speed camera is a prerequisite in μ PIV applications because of the magnified measurement plane causing the virtual magnification of the real velocities.

In the interlaced format, first all the odd rows of the image frame are read out and then all the even rows. This introduces a series of complications in PIV applications. In order to avoid these complications, other architectures are recommended such as the frame transfer and the full frame interline transfer architecture. In the **frame transfer architecture** the camera sensor is divided into two different rectangular areas: 1) the active or light sensitive area used for image acquisition and 2) the inactive or masked storage area used for the temporal storage of each acquired image. In the **full frame interline transfer architecture** the masked area is composed of columns between the active columns of the sensor.

The original advantage of the frame transfer architecture was the 100% fill factor i.e. the absence of gaps between pixels. In contrast, full frame interline transfer cameras had always fill factors much less than 100%. Later, this disadvantage was almost eliminated by using micro lenses in front of the sensor.

The **sensitivity** of a Digital μ PIV camera should be enough to acquire images of the tracer particles flowing inside the microstructure. This is not so trivial to estimate because it depends on many factors such as frame rate, exposure time and the wavelength depended factors of quantum efficiency (QE) and noise equivalent exposure (NEE).

In **CMOS (Complementary Metal Oxide Semiconductor)** cameras, photodiodes are used for detecting light instead of potential wells. A relatively new development is active pixel sensor (APS) technology which allows the integration of amplification on each pixel with an appropriate MOS-FET transistor. In a typical APS implementation **each pixel** consists of a photodiode and 3 transistors: a reset transistor to control integration time, a readout amplifier transistor (source follower) and a row select transistor.

Advantages of the **CMOS sensors in comparison to the CCD sensors** are the recording of high contrast images without blooming, higher pixel rates (less clock pulses per pixel read out) leading to higher frame rates at the same resolution, electronic shuttering integrated in each pixel (shutter transistor) and windowing (reading smaller windows of the sensor array

at higher frame rates). More details on digital cameras can be found elsewhere (Holst, 1998; Raffel et al., 2007).

2.4 Software

According to the PIV method, successive recorded images of the flow field in the (x,y) measurement plane are divided into rectangular areas called “interrogation windows” (figure 9). The time interval Δt between the recorded images is defined by the frame rate of the digital camera.

The record of the successive images of the flow in the measurement plane can form “pairs”: the first pair includes the first image and the second image after Δt , the second pair includes the second and third image, etc. Each image pair corresponds to a collection of interrogation window pairs.

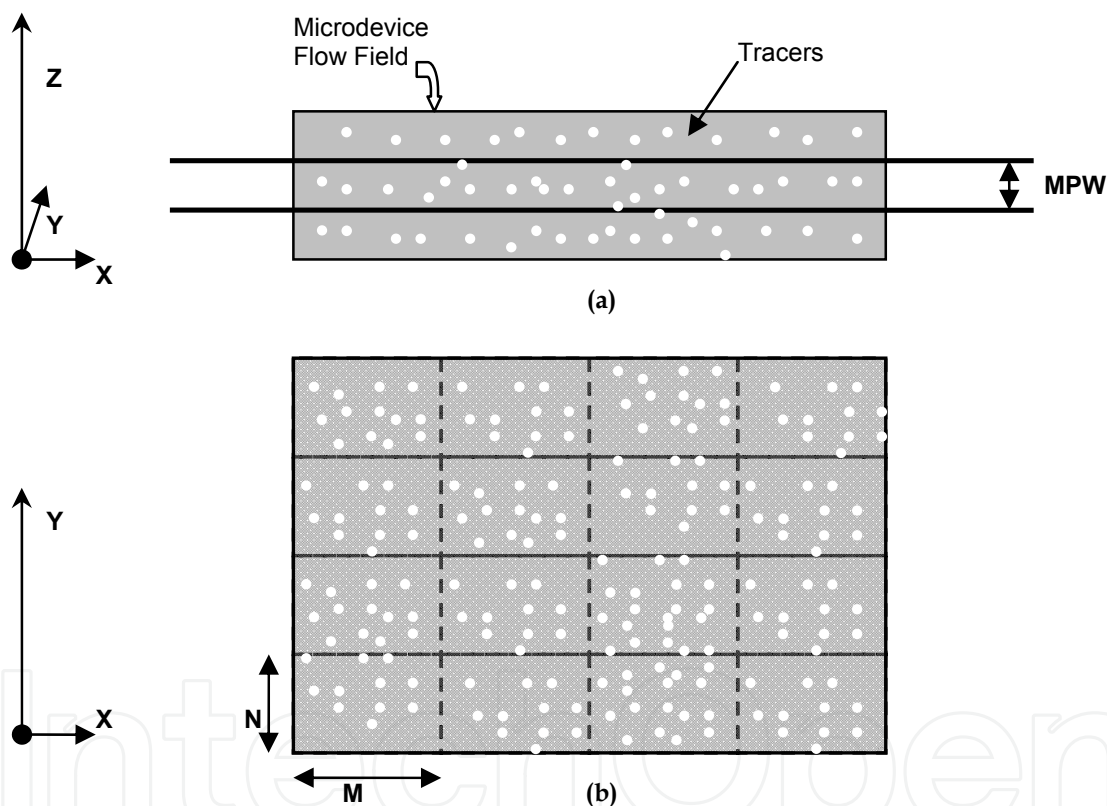


Fig. 9. **(a)** Side view of the measurement plane (x,y) . The measurement plane width (MPW) here is defined along the z axis. **(b)** Top view of the measurement plane (x,y) with the interrogation windows shown in dashed line. The size of each interrogation window in this figure is $M \times N$ pixels.

The PIV method is based on the following assumptions: **1)** the average velocity of the fluid inside every interrogation window is accurately described by the average velocity of the particle tracers inside the same window, **2)** the average particle velocity inside every window can be found by calculating the average particle displacement S caused by the flow in and **3)** the average particle displacement S can be estimated using the correlation function on the 2 window particle images.

In more detail, let's take an interrogation window pair and assume that $f(x,y)$ is the luminous intensity distribution of the first window and $g(x,y)$ the distribution in the second. Then, the cross correlation function is given by the formula:

$$\text{CCOR}(s_x, s_y) = \iint f(x,y)g(x+s_x, y+s_y)dx dy \quad (11)$$

Where (s_x, s_y) is the variable vector s coordinates of the new CCOR window (figure 10). Assuming that the interrogation windows of the first and second image have the same dimensions $M \times N$ pixels (Fig. 9(b)), then the CCOR result window will have dimensions $(M+M-1) \times (N+N-1) = (2M-1) \times (2N-1)$ pixels. For negative images, the CCOR function will have a maximum value (peak) at position $(s_{x\text{MAX}}, s_{y\text{MAX}})$ where the image of the particles in the first window coincides with the image of the particles in the second window. The CCOR peak is shown in white color in figure 10. The **vector distance S_M between the geometrical center of the CCOR window and the peak of the CCOR function** corresponds to the statistical mean displacement of the window particles.

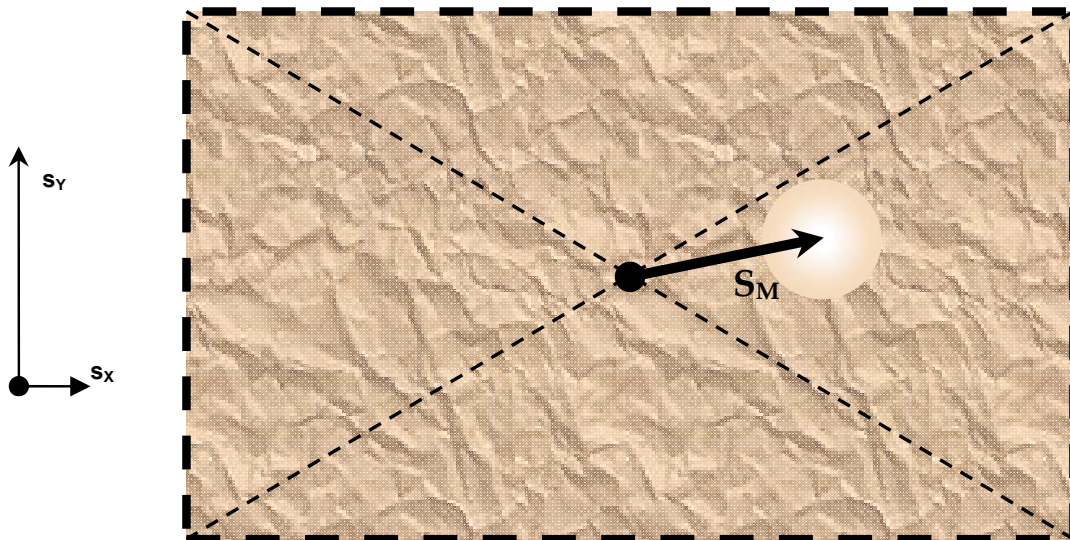


Fig. 10. The displacement vector S_M , starts from the geometrical center of the **CCOR window** and ends at the peak of the CCOR function shown in white. In the rest area of the window various values of the CCOR function are shown in dark color. Any other peak of the CCOR function giving a false estimate of the vector S is considered as "noise". The higher the difference of the "white" CCOR peak from the second highest peak, the higher the signal to noise ratio.

By analogy, when the original images are **positive** (Fig. 7 & 8), we are interested in the location of the **CCOR minimum** in order to estimate the vector distance S between the geometrical center of the CCOR window and the minimum of the CCOR function.

In a perfect situation of a white particle on a completely black background of the first window, the size of the CCOR window permits the detection of a displacement equal to $M-1$ pixels in the x direction and to $N-1$ pixels in the y direction. However, these conditions are never met in real experimental conditions with many "gray" particles from which some are lost between the first and second window. Therefore, the statistical correlation estimator CCOR has 3 components (Keane & Adrian 1992):

$$CCOR(s) = CCOR_D(s) + CCOR_C(s) + CCOR_F(s) \quad (12)$$

Where $CCOR_D$ is the displacement component (the peak of which we want), $CCOR_C$ is the mean intensity convolution component and $CCOR_F$ is the component of the convolution of the mean intensity of the first window with the fluctuating intensity of the second window. The components $CCOR_C$ and $CCOR_F$ are considered as “noise” creating a fluctuating background shown as a dark background in figure 10.

Since the computation of the cross correlation function in the space domain is time consuming, it is usually estimated in the frequency domain by using the **Fast Fourier Transform (FFT)**. Using the FFT algorithmic technique, the calculation of the CCOR is at least 10 times faster, depending on the information content of the interrogation windows. In some applications it can be 100 times faster. The shortcoming is that the CCOR window has now the same dimensions with the interrogation windows and consequently the dynamic range of the measured displacements is reduced.

Using a Gaussian interpolation in the determination of the cross correlation peak, **subpixel accuracy** can be achieved (Willert & Gharib, 1991) in the estimation of the S_M magnitude. Then a **conversion factor (CF)** measured in $\mu\text{m}/\text{pixel}$ is needed to transform the pixel units of S_M to micrometers. Since the nominal magnification of a video microscopic system often deviates from reality, an object micrometer is the best way for the CF determination.

Knowing the time interval Δt between the two successive images from the frame rate of the camera, the statistical mean velocity V corresponding to each interrogation window pair can be estimated from the classical velocity definition:

$$V = \frac{S_M}{\Delta t} \quad (13)$$

Repeating the procedure described in the above paragraphs for all the interrogation window pairs belonging to an image pair, a computer software program can calculate the **whole velocity field**.

In the early PIV implementations many scientists preferred using the **autocorrelation (ACOR)** function on a single image with double exposure. This technique is not used frequently any more, mainly due to the fact that ACOR is a 5 component estimator (Adrian, 1991, as cited in Keane & Adrian, 1992). Two of the five components are displacement components at symmetrical positions with respect to the correlation window center. This has the following implications: **1)** directional ambiguity, **2)** increased hardware complexity to select the right displacement component and **3)** approximately double noise level in comparison to CCOR. In addition, the CCOR technique permits the second window to be larger than the first window in order to reduce the in plane loss of particles F_i . This is not possible with the ACOR function.

In a **bright field μPIV set up**, the images are positive and consequently the displacement vector S_M can be estimated by two different ways: **1)** images are inverted to their negative version and the same software algorithm described above is used and **2)** positive images are used but now there should be a difference in the algorithm: the minimum of the CCOR function is detected. In either case, the typical signal to noise ratio in a brightfield set up is

low so, some kind of image processing is usually required in order to reduce the noise level or in other words to remove the background noise (Koutsiaris et al., 1999).

3. Error analysis (Uncertainty)

Using the velocity definition equation 13, there are two major error sources contributing to the total velocity measurement error: the error Δt_e in the estimation of the time interval between two images and the error ΔS_e of the displacement calculation. The time interval error is considered negligible hence we can focus on ΔS_e . Generally, ΔS_e can be considered equal to the square root of the sum of the squares of a random (RAN) and a mean bias (BS) component:

$$\Delta S_e = \sqrt{\text{RAN}^2 + \text{BS}^2} \quad (14)$$

RAN or precision is considered proportional to the effective particle image diameter d_E and the streak length λ_s (Adrian, 1991) according to the formula:

$$\text{RAN} = c(d_E + \lambda_s) \quad (15)$$

Where c is a proportionality constant ranging between 1% and 10% depending on various experimental factors such as flow tracing, velocity gradients, non uniform illumination, CCD camera electronics, the cable and digitization noise.

Most of the factors contributing to the random component can also be sources of error for the mean bias component BS. In more detail, BS could have the following error components: **1)** flow tracing error, **2)** flow structure error, **3)** particle image generation error and **4)** interrogation procedure error.

Flow tracing error is determined by the quality of density matching between particles and fluid and the Brown motion.

Flow structure error is caused by fluid accelerations in Δt and from velocity spatial gradients inside the interrogation windows. Starting from fluid acceleration and assuming it causes a critical velocity change in time τ inside the interrogation window, then, if $\Delta t > \tau$, the result will be an integration of $\mathbf{V}(t)$ over the time difference Δt of successive images. For a proper PIV quantification of the **instantaneous velocity field**, Δt should be less than τ in all interrogation windows. The definition of the **time scale** τ depends on the application and the wanted quantification quality (temporal resolution). It should be noted that in the case of linear fluid acceleration, Δt can be equal or greater than τ as long as an average estimation of the velocity is acceptable.

In analog terms with the above paragraph, assuming that a velocity gradient causes a critical velocity change in distance δ less than the size of the window, the result would be by definition an average velocity value over the surface area of the window. For a proper PIV quantification of the **spatial velocity field**, window size should be less than δ in all interrogation windows. The definition of the **space scale** δ depends on the application and the wanted quantification quality (spatial resolution). It should be noted that in the case of a linear gradient along only a certain direction (x or y) the selection criteria of δ may be less strict.

Particle image generation error can be produced by many factors such as non-uniform illumination, out of focus particles, non-uniform scattering cross section, optical aberrations, electronic and digitization noise.

Interrogation procedure error can be produced by the size of the interrogation window, the displacement S_M estimation error and the interpolation technique for the location of the CCOR peak.

The above analysis was based on the first error quantification analysis on a μ PIV application published by Koutsiaris et al. (1999). More details on PIV uncertainty can be found in other chapters of this textbook.

4. Performance of a μ PIV system

From section 2.4 it should be obvious by now that the **spatial resolution** of the μ PIV technique is defined by the size of the interrogation windows. So, which are the factors affecting window size? **First** of all, it is the size of the flow tracer particles. The smaller the particles are the smaller the interrogation windows and the higher the spatial resolution of the μ PIV technique.

Second, it is the resolution capability of the optical system and the digital camera (electro-optical system). The higher the resolution of the electro-optical system is, the smaller the interrogation window. But the resolution of the optical system depends on its numerical aperture and the resolution of the digital camera on its pixel size. So, the higher the numerical aperture and the smaller the pixel size, the smaller the interrogation window.

Third, it is the image particle density. If window density N_i is defined as the mean number of particles per interrogation window, F_i the in plane loss of particles and F_o the out of plane loss of particles, both F_i and F_o ranging between 0 and 1, then **effective image density equals $N_i F_i F_o$** (Keane & Adrian, 1992). Since PIV is a statistical method calculating the mean velocity over the entire interrogation window, the $N_i F_i F_o$ corresponds to a detection probability. The detection probability takes maximum values for $N_i F_i F_o > 7$. For example, a $N_i F_i F_o = 5.6$ corresponds to an approximate 92% detection probability.

N_i depends on the **particle concentration (N_c)** of the fluid, assuming that particles are dispersed homogeneously in the entire volume. It has been shown empirically that a volume per volume particle concentration between 1% and 2% gives an acceptable image density. When concentration is higher than say $\approx 5\%$ agglomerates start to form and when it is lower than $\approx 0.5\%$ effective image density becomes extremely low to give an acceptable detection probability and we have a situation called low image density (LID). However, as we are going to see later in the *in vitro* and *in vivo* applications of the technique, the researchers have found clever ways to overcome these limitations.

The values of the F_i and F_o depend on the **nature of the velocity field**. Fast flows cause large displacements and “aliasing” (Westerweel, 1997) reducing the F_i and the signal to noise ratio. In addition, spatial velocity gradients cause deformations influencing detection probability (Huang et al., 1993). As a starting rule of thumb the maximum particle displacement should be less than 25% the window dimension (for both directions).

The **dynamic velocity range (DVR)** of a μ PIV system can be defined in a similar way with a macroscopic PIV system, i.e. the ratio of the maximum to the lowest velocity which can be measured (Adrian, 1997). A higher frame rate digital camera, can record images from faster flows increasing linearly the dynamic range of the system, but in μ PIV applications care should be taken with exposure time. As the frame rate increases, the exposure time should decrease accordingly to avoid streaking but there is a down limit in the exposure time depending on the power of the illumination system and the sensitivity of the digital camera.

From the above paragraphs it is evident that the size of the interrogation windows can not be reduced indefinitely. There is a lower size limit depending on many factors. Similarly, the DVR can not increase indefinitely. More details on the spatial resolution and the DVR can be found in the work of Adrian (1997).

The overall performance of a μ PIV system can be improved by using **appropriate software techniques** such as overlapping, averaging, single-pixel resolution, background removal, adaptive window shifting and image correction.

With the **overlapping** technique, new windows are defined which overlap up to a point with the old ones. For example, a 50% overlapping means that new windows occupying half the area of each old window, were introduced, doubling the number of interrogation windows along each direction (double minus one). One could argue that in this case the window size is now half, but we should keep in mind that the new windows produced by overlapping do not give new information. It is actually an interpolation technique.

The **correlation averaging** technique (or **ensemble correlation**) improves dramatically the signal to noise ratio, but it requires a steady laminar flow. The technique permits also the formation of a **background image** which can be used to remove the background noise by subtracting it from the image sample pairs. An extension of the ensemble correlation technique is the **single-pixel resolution ensemble correlation** (Westerweel et al., 2004) but it requires 1000 images or more in contrast to the 10-30 image pairs of the correlation averaging technique.

The PIV bias error can be reduced using the **adaptive window shifting** technique which requires iteration for optimum results. In adaptive window shifting, the second interrogation window of each pair is shifted proportionally to the expected average particle displacement (Forward Difference Interrogation). In an improvement of this technique called CDI (Central Difference Interrogation, Wereley & Meinhart, 2001) both windows are shifted by half the expected average particle displacement: the first interrogation window is shifted backwards and the second window is shifted forwards. Using CDI the bias error can be neglected in comparison to the random error.

The random error can be reduced using **image correction** techniques. In image correction techniques (Huang et al., 1993) image patterns in the interrogation windows are deformed in a way depending on the spatial velocity gradients. In this way, the random error is reduced and the total error becomes approximately half.

More details on software techniques can be found in other textbooks (Breuer, 2005; Nguyen & Wereley, 2002; Raffel et al., 2007).

5. Research *IN VITRO*

As it is the usual practice, the first applications of the μ PIV technique were *in vitro*. The fluorescence μ PIV set up introduced by Santiago et al. (1998) produced negative images in accordance with the classical PIV systems. The μ PIV set up introduced by Koutsiaris et al. (1999) produced positive images i.e. the background was brighter than the particles (figure 11 (a)) similar to the ordinary daylight photographs. This meant that images should be inverted before calculating the cross correlation or the software should be modified to detect the minimum of the correlation function. However, this set up was much simpler and cheaper than fluorescence set ups since it did not require the use of fluorescence apparatus (special particles, light sources, optics and low light CCD cameras).

With the use of the appropriate **image processing digital filters** one can have image inversion and simultaneous increase of the signal to noise ratio. For example, the Laplace filter (a 6×6 Kernel) shown in figure 11(c) enhances particle boundaries and removes slowly varying background shading. In addition, the same kernel helps in eliminating the out of focus particles, since the spatial frequencies corresponding to the in focus flow tracers can be maximized by adjusting the size of the filter (Koutsiaris et al., 1999). The determination of thresholds and optimum filter variable values could be the object of further research in digital image processing and digital filter design. The effects of the possible variable combinations on the μ PIV flow field accuracy have not yet been examined thoroughly.

Cylindrical microtubes (Koutsiaris et al., 1999) simulate better the flow geometry of microvessels but their construction is demanding. In addition, they require a good optical matching otherwise image optical distortions must be corrected.

Rectangular microchannels are not good models for simulating animal microcirculation, but they possess a simple geometry with minimum optical distortions. The aspect ratio (AR) of a television screen is defined as the ratio of the longest (horizontal) over the shortest (vertical) side and is always greater than 1. Keeping the same definition in rectangular microchannels, the longest (horizontal) side of the cross section is usually referred to as “width” (W) and the shortest (vertical) as “height” (H). Research groups all over the world have studied flows inside microchannels with various ARs: 1 (W = $100\mu\text{m}$, H = $100\mu\text{m}$, Lima et al., 2006), 1.7 (W = $80\mu\text{m}$, H = $48\mu\text{m}$, Kuang et al., 2009), 4 (W = $800\mu\text{m}$, H = $200\mu\text{m}$, Lindken et al., 2006; W = 20mm, H = 5mm, Timgren et al., 2008), 6.7 (W = 300mm, H = 45mm, Lima et al., 2008) and 10 (W = $300\mu\text{m}$, H = $30\mu\text{m}$, Meinhart et al., 1999).

There are several analytical solutions for the steady Newtonian flow inside a rectangular channel such as those shown by Werely & Meinhart (2005), Lima et al. (2006) and Lindken et al. (2006). All these solutions contain infinite sum terms. In addition, Werely & Meinhart (2005) reported that their analytical solution failed to capture the trends of the measured profile near the wall and that in order to amend this they used a second order polynomial fit. Lima et al. (2008) reported results in the middle plane with analytical solution errors of less than 5%. However, it seems that these errors can be reduced to less than 1.6% (more than 3 times) using an alternative model equation discussed below (see figure 15 in section 7).

In 2001, Werely and Meinhart measured the flow of deionized water around human red blood cells placed in the gap between a microscope slide and a coverslip. The same year, Gomez et al. measured for the first time the flow of water based suspensions inside a microfluidic biochip designed for impedance spectroscopy.

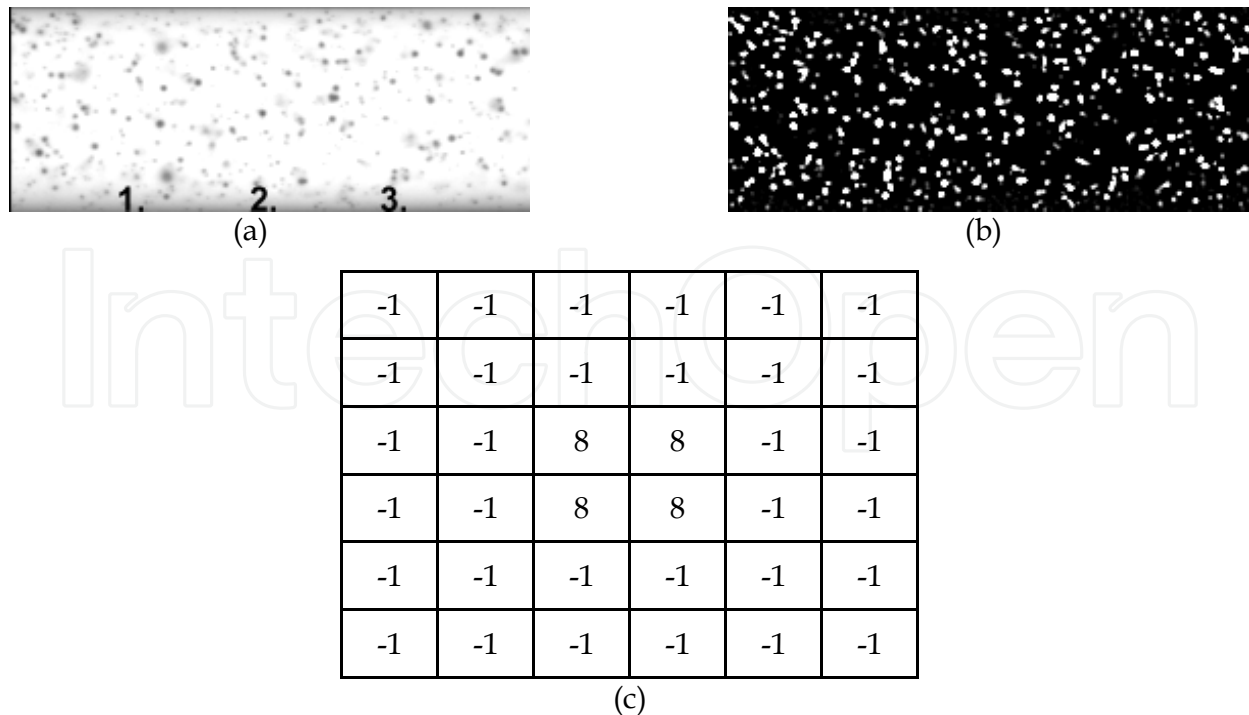


Fig. 11. (a) An original positive image from the diametric plane of a cylindrical glass tube with internal diameter of $262\ \mu\text{m}$. Numbers 1, 2 & 3 correspond to different positions downstream the flow. (b) The negative of the original image with improved signal to noise ratio, after the application of the kernel shown in (c). (From Koutsiaris et al., 1999)

Soon after the first μ PIV measurements on Newtonian flows, researchers started the flow study of **red blood cell (RBC) suspensions**. Okuda et al. (2003) measured in round tubes with internal diameter of $100\ \mu\text{m}$ the flow of rabbit blood seeded with fluorescent particles; Bitch et al., (2005) measured in specially flattened tubes the flow of a RBC suspension with 60% hematocrit using RBCs as natural flow tracers (brightfield set up).

Lima et al. (2006) were the first to measure three-dimensional velocity profiles of human RBC suspensions inside a square glass microchannel ($100 \times 100\ \mu\text{m}$) using a special confocal experimental set up. One year later (Lima et al., 2007), using the same microchannel dimensions, found that low hematocrit (up to 17%) suspensions have parabolic averaged velocity profiles. In 2008 Lima et al. compared the velocity profile of physiologic saline with the profile of human blood with 20% hematocrit inside a rectangular high aspect ratio ($W = 300\ \mu\text{m}$, $H = 45\ \mu\text{m}$) PDMS microchannel; microturbulences were encountered on averaged blood flow profiles. Next year (Lima et al., 2009), they combined a particle tracking velocimetry (PTV) system with a confocal microscope in order to quantify the RBCs trajectories in suspensions up to 20% in hematocrit.

When the tube dimension is greater than $40\text{-}60\ \mu\text{m}$ it is difficult for the light rays to penetrate blood at physiologic hematocrits both in transmission and reflectance mode. Even when a confocal set up is used, the microchannel dimension parallel to the optical axis should be less than $\approx 100\ \mu\text{m}$ and the hematocrit less than $\approx 20\%$. In order to overcome these limitations, Kim and Lee (2006) tried a completely different approach using X-rays. The Fresnel diffraction pattern images can be used to calculate the blood velocity field at high

haematocrits (20-80%) without tracer particles, in microchannels with dimensions higher than $\approx 500 \mu\text{m}$. A disadvantage of the method is that sample thickness and haematocrit affect image quality so more work is required to define the limits inside which valid measurements can be taken.

In 2011, Kaliviotis et al. used brightfield μPIV to measure the velocity field of 45% haematocrit human blood samples inside an optical shearing system consisted of 2 circular parallel glass plates set apart by a gap $h = 30 \mu\text{m}$. The shear rate derived from the blood velocity field was used in their non-Newtonian (shear rate, time and aggregation depended) blood viscosity model.

Except for the biological flows, *in vitro* μPIV has a lot of other useful applications such as those regarding the **computer industry**. Meinhart and Zhang (2000) measured the evolution of the meniscus and the detailed flow fields inside a nozzle of an inkjet printhead. Buffone et al. (2005) investigated the thermocapillary Marangoni convection in the proximity of the liquid-vapor interface for an evaporating meniscus in horizontal capillary tubes (600, 900 and 1630 μm). Today, air cooling limitations are responsible for a barrier in the total power consumed by a processor chip (a power wall of approximately 100 Watts) and ultimately in the chip performance. However, this situation can change using microchannels for liquid flow cooling (either single phase cooling with water, or two phase cooling with refrigerant). This could be a revolution in the microelectronics industry since the maximum heat dissipation can increase approximately 10 times from 37 W/cm² (air cooling) to 314 W/cm² (Thome & Marcinichen, 2011). Typical components of a two phase microcircuit are a liquid micropump or vapor compressor, a microevaporator and a microcondenser.

Among **other applications**, Bown et al., (2005) demonstrated the application of μPIV to complex microchannel geometries and introduced a method of estimating the out of plane effects on the velocity measurements. Lindken et al. (2006) measured for the first time in the mixing region of a T-shaped micromixer. King et al. (2007) demonstrated the ability to perform μPIV measurements of aqueous plugs in two phase flow within circular tubing with a 762 μm internal diameter. Such two phase flows are encountered in lab-on-chip devices designed for various biological applications such as the Polymerase Chain Reaction (PCR). Similarly, Tingren et al. (2008) measured the velocity field inside silicon oil drops forming in a mixture of water and glycerol flowing in a rectangular channel.

Kuang et al. (2009) presented a **molecular tracer method** (Molecular Tracers Velocimetry, MTV) for measuring the velocity profile in cylindrical and rectangular microchannels with dimensions less than 100 μm . Their method was based on the Laser Induced Fluorescence Photobleaching Anemometry (LIFPA) technique.

More information on the **biological applications** of μPIV can be found in the review paper of Lindken et al. (2009) and more details on the numerical and experimental analysis of flows inside microdiffusers and valveless micropumps are presented in the review paper of Nabavi (2009).

6. Velocity profile measurements *IN VIVO*

The actual measurement of the blood velocity profile in microvessels is a known difficult task to accomplish. This is in part due to the many different scientific fields that need to

cooperate and in part due to the expensive experimental set up. Therefore it is not surprising that apart from some preliminary efforts in the 70's (Schoenbein & Zweifach, 1975), the **first *in vivo*** quality velocity profile measurements were presented in 1986 by the group of professor Reneman (Tangelder et al., 1986). They measured velocity profiles in the arterioles of the rabbit mesentery using as flow tracers platelets labeled with a special fluorescence technique.

More than 15 years later, Sugii et al. (2002) and Nakano et al. (2003) measured the velocity profile in arterioles of the rat mesentery using a technique introduced some years earlier by Sugii et al. (2000) under the name "**High Resolution Particle Image Velocimetry**" (**HR-PIV**). Regarding the software, this technique was a combination of the iterative cross-correlation method (Raffel et al., 2007) and the optical flow (or gradient or spatio-temporal derivative) method, providing excellent accuracy (as little as 0.01 pixels). Their hardware was a brightfield μ PIV set up with the exceptional advantage of using natural blood flow thus avoiding any toxic effects from fluorescent materials and complex-expensive fluorescent equipment. The final velocity field spatial resolution in the object plane was 0.8 μ m. The only drawback is that being a **fully automated** technique it is difficult to validate the results. Another fully automated technique was presented by Tsukada et al. (2000) based on circular correlation windows reduced down to the size of the erythrocytes.

In 2003, Hove et al. (2003) mapped the flow field inside the developing zebrafish heart 37 hours and 4.5 days post fertilization using RBCs as flow tracers. They found the presence of higher shear vertical flow than expected and evidence that **blood flow-induced forces act as a key epigenetic factor** in embryonic cardiogenesis. Later, Vennemann et al. (2006) improved the resolution of the flow field maps and boundaries, using fluorescent, long-circulating liposomes with a diameter of 400 nm, as flow tracers, in the embryonic avian heart. They noted the potential of μ PIV to become a general tool in complex geometries in cardiovascular research. Both groups underlined the importance of examining the interplay between genetics and fluid shear forces in analyzing not only normal development but also the pathogenesis of embryonic cardiovascular defects.

In 2004, Long et al. (12 venules from male mice, $24 \mu\text{m} \leq D \leq 42.9 \mu\text{m}$) and Damiano et al (9 light-dye treated venules from 3 mice, $24 \mu\text{m} \leq D \leq 42.9 \mu\text{m}$) provided the most complete **manual** velocity profile measurements until now, with the best spatial resolution and the assumption of steady axisymmetric flow. They measured in the cremaster muscle of mice using fluorescent microspheres ($0.47 \pm 0.01 \mu\text{m}$) as blood flow tracers.

In 2005, Nakano et al. (2005) were the first to measure the effect of an arteriolar bifurcation and confluence on the red blood cell velocity profile on the rat mesentery. More recently, Potter & Damiano, (2008) performed measurements in mice venules up to diameters of 101 μ m but they mainly concentrated on the properties of the endothelium glycocalyx layer both *in vivo* and *in vitro*.

7. Velocity profile equations *IN VIVO*

7.1 Introduction

The accurate quantification of the velocity profile in a cylindrical axisymmetric flow is very important because it is the **first and unique step** required for the estimation of the wall

shear rate (WSR) and volume flow (Q). In addition, the viscosity profile (and hence the apparent viscosity), the axial pressure gradient and the shear stress profile (and hence wall shear stress, WSS) can be estimated **under the assumptions** of a locally Newtonian fluid and the existence of plasma between red blood cells (RBCs) and vessel walls (Damiano et al., 2004).

Before the last third of the 20th century, the only equation available to the researchers studying laminar flows inside cylindrical tubes was the parabolic one. In the seventies (70s) it became evident that the flow of blood is quite different from simple Newtonian flows like that of water. Blood exhibits special shear thinning properties due to reasons which are still partly unexplained. For example the molecular and biochemical basis of the rouleaux (structures resembling coin piles) formation is still unknown. The shear thinning property means that blood viscosity diminishes (blood becomes thinner) as shear rate increases. For the case of blood, this property is quite evident taking into account that at high shear rates ($> 100 \text{ s}^{-1}$) its viscosity is many times lower than at shear rates $< 10 \text{ s}^{-1}$. This means that near the vessel axis where there are such low shear rates, blood is much more viscous, causing a characteristic “blunting” of the velocity profile (Bugliarello & Sevilla, 1970; Damiano et al., 2004; Gaehtgens et al., 1970; Long et al., 2004; Nakano et al., 2003; Schoenbein & Zweifach, 1975; Tangelder et al., 1986).

After 1970, the researchers proposed equations trying to describe the blunting of the velocity profile in the microvasculature with diameters (D) higher than $\approx 20 \mu\text{m}$. The approximate diametric **down size limit of the 20 μm** (Cokelet, 1999) is imposed by the manifestation of the biphasic nature of blood in the smallest arterioles and venules and in the capillaries. In these microvessels RBCs flow separately, constituting a different liquid phase from plasma and therefore the flow medium can not be considered as a “continuum” and a velocity profile can not be defined in the ordinary sense. However, **averages of WSR, Q and WSS** can be estimated *in vivo* using empirical equations (Koutsiaris, 2005; Koutsiaris et al., 2007) requiring only axial RBC velocity measurements.

The available velocity profile equations today, could be divided in many ways, but in this section the criterion was whether they can be easily reduced to the classic parabolic equation (Group A) or not (Group B).

7.2 Available equations

Realistic assumptions of the blood flow in straight sections of microvessels with $D > 20 \mu\text{m}$, several diameters downstream their entrance, are (Koutsiaris, 2009): 1) incompressible flow, 2) continuous medium, 3) viscous flow with Reynolds number less than one, 5) cylindrical vessel geometry with a radius R, 5) non-Newtonian medium with a time averaged velocity profile blunter than the parabolic with the same maximum velocity V_m , 6) the blood velocity is zero on the vessel wall (zero slip condition: $V(r) = 0$, at radial position $r = R$) and 7) axisymmetric velocity profile with maximum velocity V_m on the vessel axis.

The assumption of steady flow can be accepted for venules with $D > 20 \mu\text{m}$ (Koutsiaris et al., 2011), but not for arterioles. Recently, it was verified for the first time in humans, that the velocity pulse in arterioles is quite strong, even at the precapillary level (Koutsiaris et al., 2010c). Despite the strong pulse, the velocity profile can be measured at the same cardiac cycle phase taking advantage of the periodic nature of the flow. So, the flow can be considered as “steady” for the same phase.

All the above conditions are satisfied by the equations presented below except for the parabolic equation which can not satisfy the non-Newtonian condition, as it will be shown below.

7.2.1 Group A

This group comprises 3 velocity profile equations:

$$V_P(r) = V_m \left[1 - \left(\frac{r}{R} \right)^2 \right] \quad (16)$$

$$V_{RS}(r) = V_m \left[1 - \left(\frac{r}{R} \right)^\kappa \right] \quad (17)$$

$$V_{KS}(r) = V_m \left[1 - \kappa_1 \left(\frac{r}{R} \right)^2 \right] \left[1 - \left(\frac{r}{R} \right)^{\kappa_2} \right] \quad (18)$$

Where $V_P(r)$, $V_{RS}(r)$, $V_{KS}(r)$ is the velocity at radial position r , for the parabolic (equation 16), the Roevros (equation 17, Roevros 1974) and the Koutsiaris (equation 18, Koutsiaris 2009) equation, respectively.

The parameters κ and κ_1 , κ_2 **affect the velocity profile shape** of equations 17 and 18 respectively. For a velocity profile blunter than the parabolic one, with the same V_m , the following conditions must be satisfied: $\kappa > 2$ (equation 17), $0 < \kappa_1 < 1$, $\kappa_2 > 2$ and $(1-\kappa_1) \kappa_2 \geq 2$ (equation 18).

In **equation 17**, the higher the κ , the flatter the profile near the vessel axis and the higher the wall shear rate (Roevros 1974). Equation 17 reduces to parabolic when $\kappa = 2$. It should be noted that a modified version of equation 17 with 2 more parameters (a and b) was proposed in the 80s (Tangelder et al., 1986), but it does not satisfy the zero slip condition on the vessel wall which is true for any viscous flow.

In **equation 18**, the advantage is that the bluntness of the profile can be controlled near the axis and the wall: generally, as κ_1 approaches zero the profile becomes flatter near the axis and as κ_2 takes values higher than 2 the profile becomes flatter near the wall (Koutsiaris, 2009). Equation 18 reduces to the parabolic equation when $\kappa_1 = 0$, $\kappa_2 = 2$.

7.2.2 Group B

Damiano et al. (2004) made significant contributions in theory and experimental measurements and provided a way to estimate the viscosity profile as well as the effective viscosity *in vivo*. They proposed the following velocity profile equation which identically satisfies the momentum equation and boundary conditions (Long et al., 2004):

$$V(r) = V_m \frac{\int_0^R f(\sigma) d\sigma}{\int_0^R f(\sigma) d\sigma} \quad (19)$$

Where $f(\sigma)$ is a function of R and of two independent parameters c_1 and c_2 which can be found through non linear regression analysis that uses equation 19 to minimize the least-squares error (SSE) of the fit to the experimental velocity profile data sets (Long et al., 2004). With a suitable modification the equation can take into account the infinitesimal flow inside the microvascular glycocalyx layer. This is important for the transcapillary exchange and endothelium studies but from the volume flow estimation point of view it contributes little due to the very low velocities near the vessel wall. The fitting of this equation to experimental data from mouse venules can be seen in the relevant papers (Damiano et al., 2004; Long et al., 2004).

7.3 Fitting efficiency

At a preliminary evaluation of the **group A equations** (Koutsiaris et al., 2010a), fixed values for the parameters were selected: $\kappa = 9$ (equation 17) and $\kappa_1 = 0.58$, $\kappa_2 = 22$ (equation 18) assuming they all have the same axial velocity estimated from the nearest experimental point to the vessel axis (**axial fit**). Eight profiles from **mouse venules** were estimated **graphically** from the literature (Long et al., 2004). According to the results, the parabolic equation tends to underestimate blood velocity, reaching a maximum relative error of - 72% near the vessel wall. The Røevros equation tends to overestimate blood velocity reaching a maximum relative error of + 48% at a radial position between 70% and 80% of the vessel radius R . Equation 18 tends to approximate blood velocity with a relative error between - 8% and + 7%, for all radial positions, leading to an average volume flow error of less than 0.5%. An axial fit example of the 3 equations is shown in figure 12.

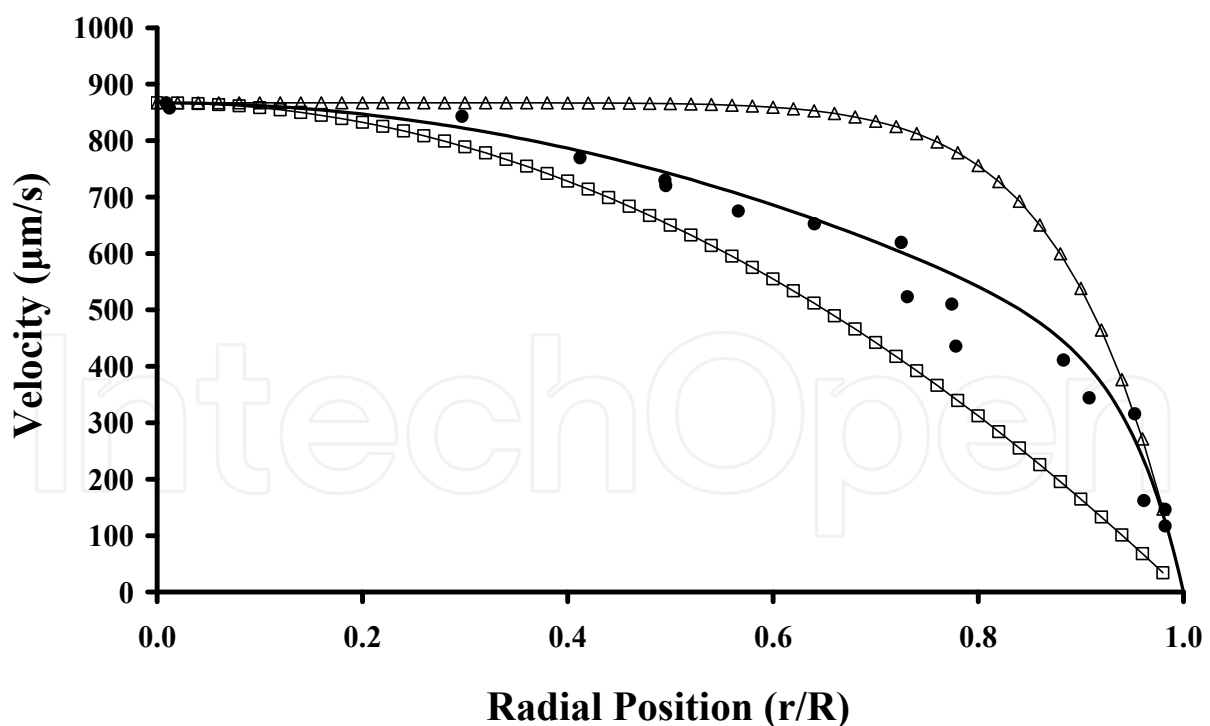


Fig. 12. Velocity profile equation 16, 17 and 18 (with the same axial velocity V_m) is shown in squares, triangles and solid black line respectively (Koutsiaris et al., 2010a). Velocity profile data from a 38.6 μm mouse venule are shown in black dots. Data were estimated graphically from Long et al. (2004).

Instead of using the same maximum velocity and fixed parametric values (axial fit), the classical approach would be to apply the **best fit**, i.e. finding the parametric values producing the minimum sum square error on each experimental velocity profile. Then statistics could be applied to the velocity relative errors of all the profiles, dividing the normalized radial position (r/R) at 10 different radial segments:

$$\frac{j-1}{10} \leq \frac{r}{R} \leq \frac{j}{10} \quad (20)$$

Where j is an integer index ($1 \leq j \leq 10$). Working in this way, Koutsiaris et al. (2011) compared statistically the best fits of equations 17 and 18 and the axial fit of equation 18 on the **original experimental data of 12 velocity profiles from mouse venules** between 21 and 39 μm in diameter (Long et al., 2004). As it is shown in figure 13, the most efficient fit is the best fit of equation 18 with average relative errors (RE_j) between -1% and +2% in all radial segments, but it requires the complete velocity profile data from each vessel. The axial fit of equation 18 gives results with acceptable error (RE_j less than 11%) and requires only one velocity measurement near the vessel axis (Koutsiaris, 2009; Koutsiaris et al., 2011).

Here, it should be noted that a lot of researchers working in the area of micro blood flow still use the parabolic equation. As it is proved by figures 12 and 13, according to the current experimental data, the parabolic equation can lead to serious errors, especially near the vessel wall.

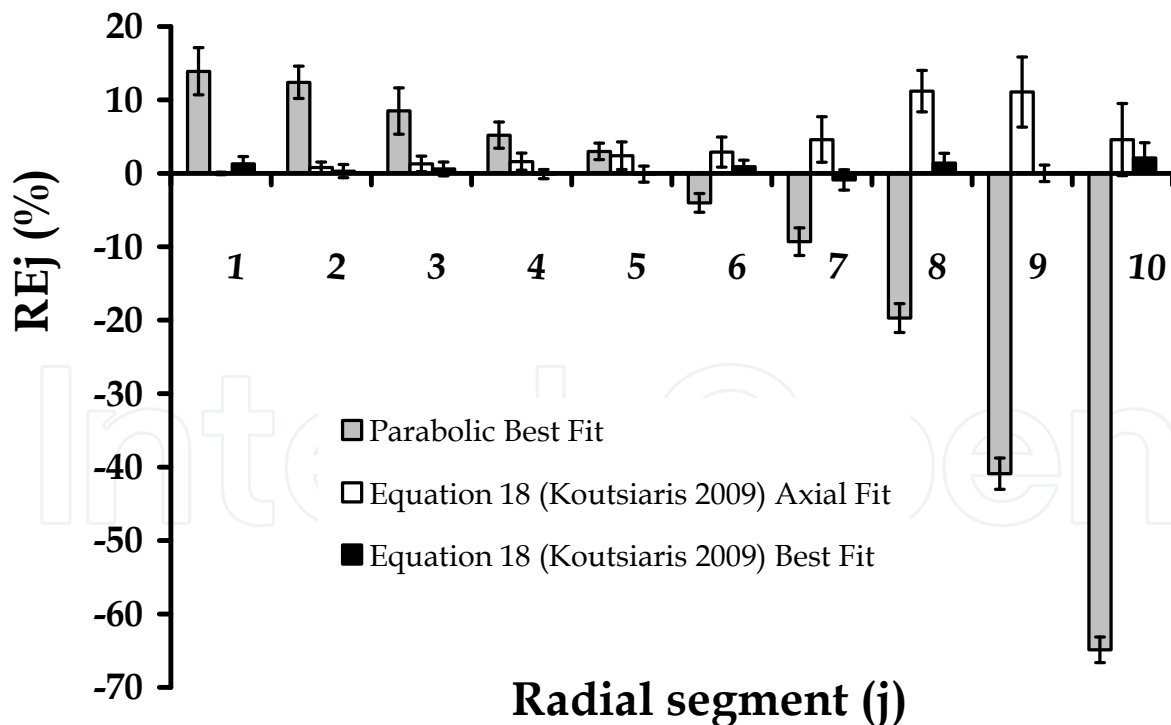


Fig. 13. Velocity **relative error (RE)** statistics on original experimental data from the mouse cremaster muscle (12 velocity profiles, Long et al., 2004). **Average RE of each segment j (RE_j)** is shown in columns and standard error of the mean is shown with black bars on each column. Gray, white and black columns represent the parabolic best fit, the equation 18 axial fit and the equation 18 best fit respectively. Data were taken from Koutsiaris et al. (2011).

In addition, it should be noted that the best fit of the Røevros equation was not examined here, because it has already been reported (Tangelder et al., 1986) that it tends to underestimate velocity in the center of the vessel and near the wall and to overestimate velocity in the range $0.5 \leq (r/R) \leq 0.8$.

As it was mentioned in the beginning of section 7.2, equations 16 to 19 could also be applied to the same phase of the **arteriolar blood flow**. The best fit of equation 18 to the **original velocity profile data** from a 25 μm rabbit arteriole at the diastolic phase (Tangelder et al., 1986) is shown in figure 14. The dispersion of the 151 experimental points around the black line in figure 14 (a) was caused by at least two factors: **1)** the inability of a volume illuminated system to define the measurement plane (out of focus effects) and **2)** small irregularities in the periodic arteriolar flow.

The first obstacle can now be overcome with modern confocal systems (section 2.2.6). An off-line way to overcome the out of focus effects is the use of the filtering criterion proposed by Damiano et al. (2004). The best fit of equation 18 on the 11 experimental points left after applying this criterion is shown in figure 14 (b).

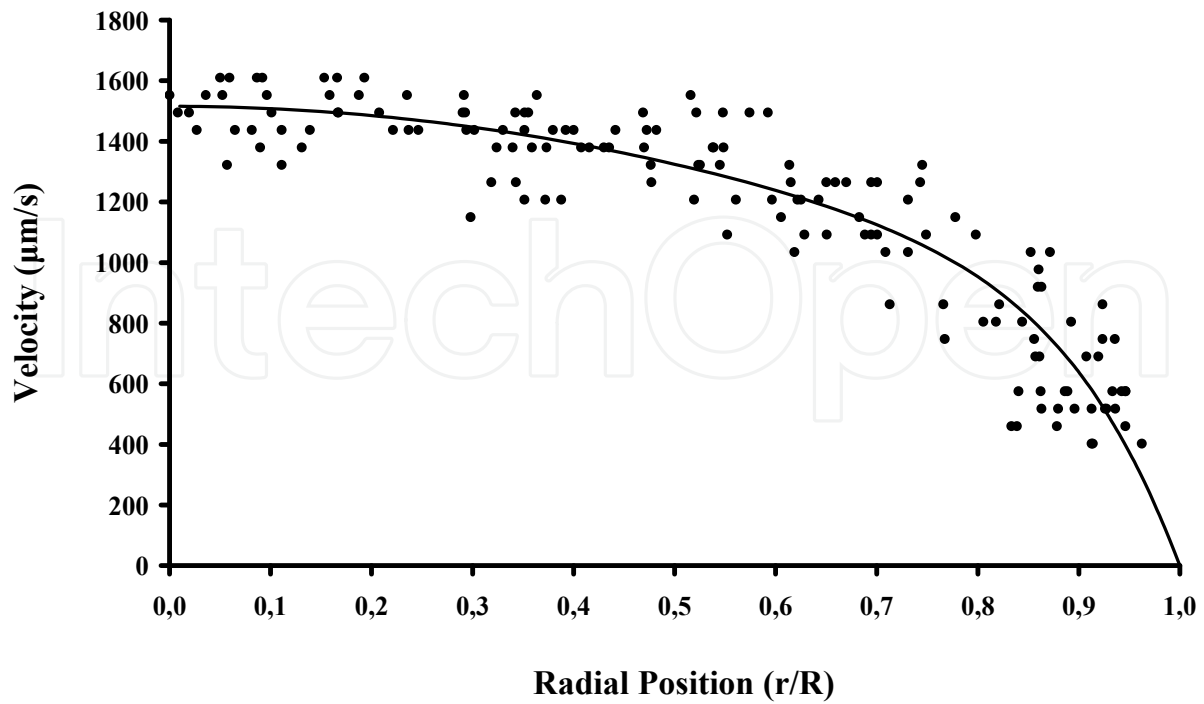
Closing this section, it should be reported that equation 18 seems also to provide good fits, to velocity profile data coming from **Newtonian fluids inside rectangular microchannels**. It appears that rectangular cross sections with aspect ratios $\gg 1$ (or $\ll 1$ depending on the definition; here the definition described in section 5 was accepted) distort the parabolic velocity profile of a Newtonian fluid producing blunt profiles similar to those of shear thinning fluids, such as blood, flowing inside cylindrical microchannels. The blunt profiles of the Newtonian fluids appear along the greatest side of the rectangular cross section.

An example of velocity profile along the greatest dimension (width W) of a rectangular cross section microchannel is shown in figure 15. The width was defined along the y direction, the height (H) was defined along the z direction and the length along the x direction (the direction of flow). The experimental velocity profile data shown in black dots, were measured in the central plane ($z = (H/2) = 22.5 \mu\text{m}$, Lima et al., 2008) and the width position y here was normalized with $(W/2) = 150 \mu\text{m}$. The line represents the best fit approximation of equation 18. The parametric values of equation 18 giving the best fit were: $V_m = 0.451 \text{ mm/s}$, $\kappa_1 = 0.109$ and $\kappa_2 = 12$. The κ_2 value was rounded down to the nearest even number, because a non-positive number can not be raised to a fractional power. Even with this approximating κ_2 value, the absolute relative error ($|RE|$) was less than 1.6% and the average $|RE|$ was 0.5%.

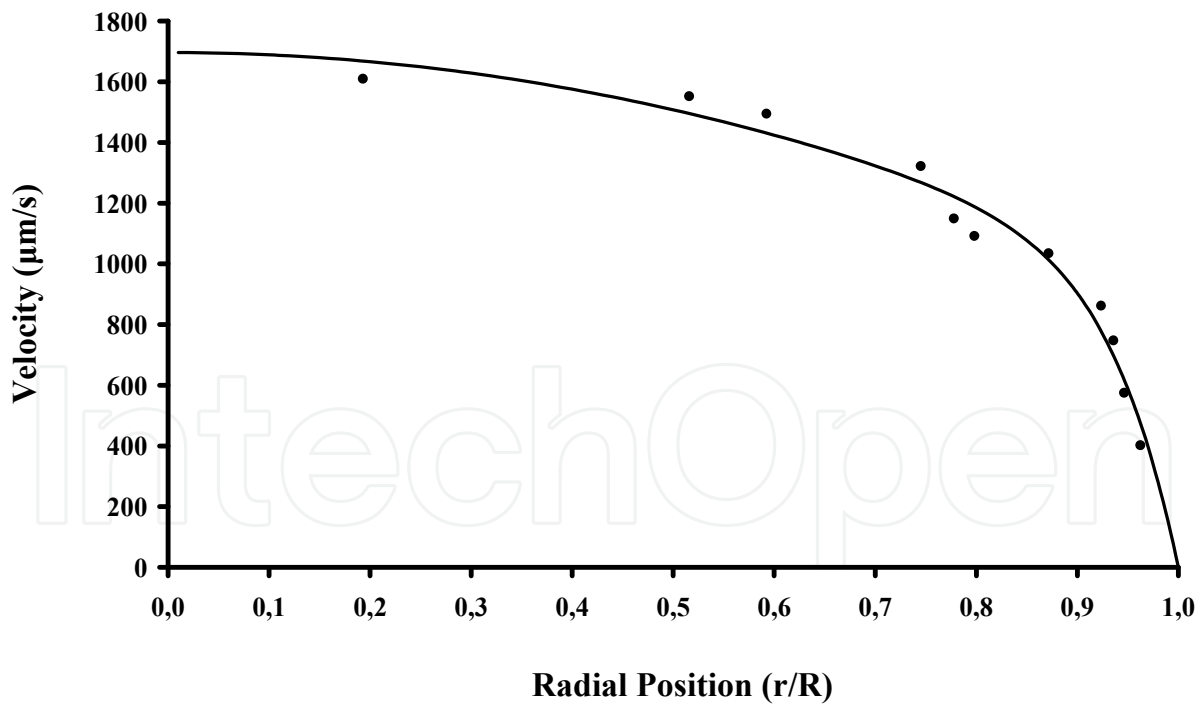
Perhaps, the parameters κ_1 and κ_2 could be expressed as functions of the aspect ratio (W/H) and the z position in order to use equation 18 for the velocity profile expression of a Newtonian fluid in every rectangular channel, but this requires more experimental data at various aspect ratios in order to be verified.

7.4 Application to humans

A fundamental remaining question is whether equation 18, which seems to approximate efficiently the blood velocity profile in the mouse and rabbit microcirculation, can be applied to the human microcirculation also. Taking into account the current state of technology, it would be rather difficult now, or in the near future, to measure the velocity profile of blood in human microvessels.



(a)



(b)

Fig. 14. Best fit of equation 18 to original velocity profile data from a 25 μm rabbit arteriole at the diastolic phase (Tangelder et al., 1986). (a) 151 experimental points. (b) 11 experimental points after filtering.

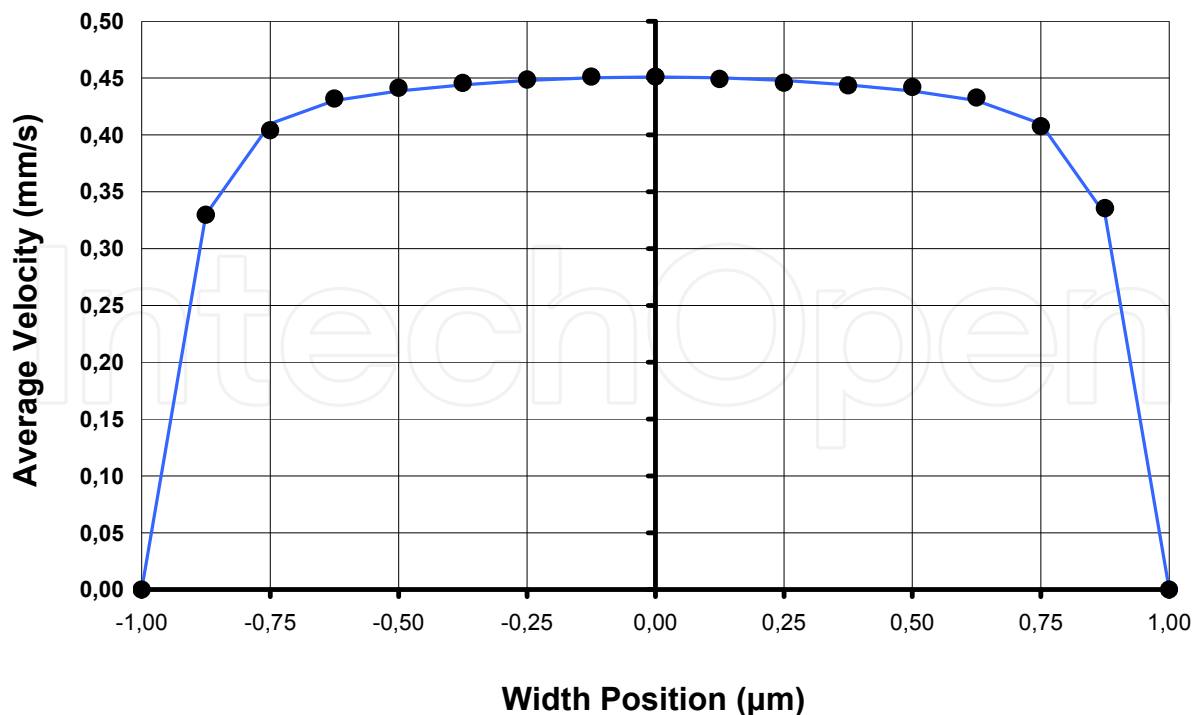


Fig. 15. Best fit of equation 18 (shown with a line) to velocity profile data (shown with black dots) from a rectangular microchannel (Lima et al., 2008, Fig. 5) with a Height (H) = 45 μm and a Width (W) = 300 μm . Here, the width position was normalized with $(W/2) = 150\mu\text{m}$. The absolute relative error of the fit was less than 1.6% at all experimental points.

An indirect way of finding the answer would be to measure the rheological differences between mouse and human blood and more specifically the viscosity differences at low shear rates. In case these differences prove to be high enough, presumably the profiles would be different and a change of the equation fixed parametric values would be required.

It is already known (Windberger et al., 2003; Windberger & Baskurt, 2007) that in humans and other athletic species like horses, **whole blood viscosity (WBV)** is higher than in mice. However, this WBV difference becomes important at very low shear rates ($< 10 \text{ s}^{-1}$) occurring close to the vessel axis. Using the fixed parametric form of equation 18, the shear rate of 10 s^{-1} corresponds to a radial position $r = 0.18 R$, or to a surface area of only 3.3% of the total cross sectional area of the vessel. Therefore, it would be logical to assume that the fixed parametric form of equation 18 could be applied to the human microvessels as well. However, one could argue that this region near the vessel axis was responsible for the profile blunting in the first place.

A more detailed viscometric experiment comparing mouse and human blood samples would involve WBV measurements at many different shear rates $< 10 \text{ s}^{-1}$, at physiologic temperatures (human blood at 36.6 °C and mouse blood at 38 °C). Even so, there would be some remaining issues such as the use of anticoagulants in the blood samples and the selection of the appropriate hematocrit level, since according to the Fahraeus effect, the average microcirculatory hematocrit is lower than the systemic hematocrit (H_s). As it was proved by Lipowsky et al. (1980), for diameters of approximately 20 μm , the average hematocrit *in vivo* would be approximately 0.28 H_s in the venous side. A suggested set of experiments would comprise WBV measurements at hematocrits of 0.28 H_s , 0.38 H_s and 0.50 H_s .

8. Conclusion

In this chapter a medium size review was given on digital micro particle image velocimetry (μ PIV). The four main components of a Digital μ PIV system were described in subsections of section 2: 2.1) microfluidics, 2.2) optics, 2.3) electronics and 2.4) software.

In the optics subsection, important insight was given into the concepts of volume illumination, depth of focus (DoF), f number (f#), measurement plane width (MPW) and effective diameter (d_E). In addition, the distinction between fluorescent and brightfield μ PIV systems was clarified.

The latest development in μ PIV optics is the “confocal” experimental set up which has the advantage of defining the width of the measurement plane (optical slice thickness). It seems that this will be the long term future of the digital μ PIV set ups. However, at the moment, this is an expensive solution and there is always the drawback of the single point scanning, meaning that the image of the measurement plane is not strictly acquired at the same time. It is the view of the writer that low cost brightfield systems have not been examined adequately together with the use of image processing techniques.

In the electronics subsection some hints were given on digital camera species and architecture. In the software subsection the basic algorithm was described together with the basic assumptions and differences between fluorescent and brightfield set ups.

In addition, a brief but incisive description was given of the error (uncertainty, section 3) and performance (section 4) of a μ PIV system, two subjects that often are not given the proper attention.

The promising future of the Digital μ PIV technique stems from the wide range of applications in micromechanics and microelectronics industry and research. Separate sections (sections 5 and 6) were devoted to the *in vitro* and *in vivo* experiments with a historical research overview.

Special emphasis was given on the microflows of biological fluids and especially in the velocity profiles of blood *in vivo*. A separate section (section 7) was dedicated on the velocity profile equations *in vivo* and their evaluation based on original experimental data.

All current experimental evidence suggests that the classical parabolic velocity profile is inappropriate for describing blood flow in the mammalian microvasculature. As it was shown in section 7, there are now **new equations** and **fitting techniques** for the expression of the average velocity profile of small mammals *in vivo* with acceptable error (figures 12, 13 and 14). In conclusion these new equations are at the moment the best choice for the description of blood flow in the human microcirculation. It should also be noted that equation 18 seems to describe well the Newtonian flow inside rectangular microchannels.

9. Acknowledgments

The author of this chapter would like to thank Professor Edward Damiano from Boston University, USA, Professor Geert Tangelder from VU University Medical Center, Amsterdam, The Netherlands and Professor Rui Lima from Polytechnic Institute of Braganca, Portugal, for kindly sending the necessary original experimental data.

10. References

- Adrian, R.J. (1991). Particle-imaging techniques for experimental fluid mechanics. *Annu. Rev. Fluid Mech.*, Vol.23, pp. 261-304, ISSN 0066-4189.
- Adrian, R.J. (1997). Dynamic ranges of velocity and spatial resolution of particle image velocimetry. *Meas. Sci. Technol.*, Vol.8, pp. 1393-1398, ISSN 0957-0233.
- Bitsch, L.; Olesen, L.H.; Westergaard, C.H.; Bruus, H.; Klank, H. & Kutter, J.P. (2005). Micro particle-image velocimetry of bead suspensions and blood flows. *Exp. Fluids*, Vol.39, pp. 505-511, ISSN 0723-4864.
- Bourdon, C.J.; Olsen, M.G. & Gorby, A.D. (2004). Validation of an analytical solution for depth of correlation in microscopic particle image velocimetry. *Meas. Sci. Technol.*, Vol.15, pp. 318-327, ISSN 0957-0233.
- Bown, M.R.; MacInnes, J.M. & Allen, W.K. (2005). Micro-PIV simulation and measurement in complex microchannel geometries. *Meas. Sci. Technol.*, Vol.16, pp. 619-626, ISSN 0957-0233.
- Bown, M.R.; MacInnes, J.M. & Allen, W.K. (2006). Tree-component micro-PIV using the continuity equation and a comparison of the performance with that of stereoscopic measurements. *Exp. Fluids*, Vol.42, pp. 197-205, ISSN 0723-4864.
- Breuer, K. (Ed.). (2005). *Microscale Diagnostic Techniques*, Springer, ISBN 3-540-23099-8, Heidelberg.
- Buffone, C.; Sefiane, K. & Christy, J.R.E. (2005). Experimental investigation of self-induced thermocapillary convection for an evaporating meniscus in capillary tubes using micro-particle image velocimetry. *Physics of Fluids*, Vol.17, No 5, pp. 052104/1-18, ISSN 1070-6631.
- Bugliarello, G. & Sevilla, J. (1970). Velocity distribution and other characteristics of steady and pulsatile blood flow in fine glass tubes. *Biorheology*, Vol.7, pp. 85-107, ISSN 0006-355X.
- Chrobak, K.M.; Potter D.R. & Tien, J. (2006). Formation of perfused, functional microvascular tubes in vitro. *Microvasc. Res.*, Vol.71, pp. 185-196, ISSN 0026-2862.
- Cokelet, G.R. (1999). Viscometric *in vitro* and *in vivo* blood viscosity relationships: how are they related? *Biorheology*, Vol.36, pp. 343-358, ISSN 0006-355X.
- Damiano, E.R.; Long, D.S. & Smith, M.L. (2004). Estimation of viscosity profiles using velocimetry data from parallel flows of linearly viscous fluids: application to microvessel haemodynamics. *J. Fluid Mech.*, Vol.512, pp. 1-19, ISSN 0022-1120.
- Delly, J.G. (1988). *Photography through the microscope*, Eastman Kodak Company, ISBN 0-87985-362-X, New York, USA.
- Gad-el-Hak, M. (Ed.). (2005). *The MEMS Handbook* (2nd Edition, 3 Volume Set), CRC press (Taylor & Francis Group), ISBN 0-84932-106-9, Florida, USA.
- Gaehtgens, P.; Meiselman, H.J. & Wayland, H. (1970). Velocity profiles of human blood at normal and reduced hematocrit in glass tubes up to 130 μ Diameter. *Microvascular Research*, Vol.2, pp. 13-23, ISSN 0026-2862.
- Gardel, M.L.; Valentine, M.T. & Weitz, D.A. (2005). Microrheology, In: *Microscale Diagnostic Techniques*, Breuer K.S. (Ed.), pp. 1-49, Springer, ISBN 3-540-23099-8, Heidelberg.
- Gomez, R.; Bashir, R.; Sarakaya, A.; Ladisch, M.R.; Sturgis, J.; Robinson, J.P.; Geng, T.; Bhunia, A.K.; Apple, H.L. & Werely, S.T. (2001). Microfluidic biochip for impedance spectroscopy of biological species. *Biomed. Microdevices*, Vol.3, No 3, pp. 201-209, ISSN 1387-2176.

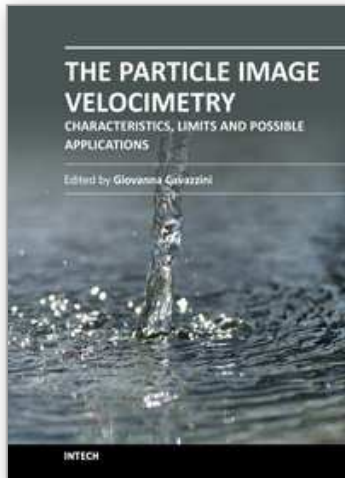
- Hassan, I. (2006). Thermal-Fluid MEMS Devices: A Decade of Progress and Challenges Ahead. *J. Heat Trans-T ASME*, Vol.128, No.11, pp. 1221-1233, ISSN 0022-1481.
- Holst, G.C. (1998). *CCD arrays cameras and displays*, SPIE Press, ISBN 0-8194-2853-1, Bellingham, Washington, USA.
- Hove, J.R.; Köster, R.W.; Forouhar, A.S.; Acevedo-Bolton, G.; Fraser, S.E. & Gharib, M. (2003). Intracardiac fluid forces are an essential epigenetic factor for embryonic cardiogenesis. *Nature*, Vol.421, pp. 172-177, ISSN 0028-0836.
- Huang, H.T.; Fiedler, H.F. & Wang, J.J. (1993). Limitation and improvement of PIV, part II. Particle image distortion, a novel technique. *Exp.Fluids*, Vol.15, pp. 263-273, ISSN 0723-4864.
- Kaliviotis, E.; Disting, J. & Balabani, S. (2011). Spatial variation of blood viscosity: Modelling using shear fields measured by a μ PIV based technique. *Medical Engineering & Physics*, Vol.33, pp. 824-831, ISSN 1350-4533.
- Kean, R.D. & Adrian, R.J. (1992). Theory of cross-correlation analysis of PIV images. *Applied Scientific Research*, Vol.49, pp. 191-215, ISSN 1386-6184.
- Kim, G.B. & Lee, S.J. (2006). X-ray PIV measurements of blood flows without tracer particles. *Exp. Fluids*, Vol.41, pp. 195-200, ISSN 0723-4864.
- King, C.; Walsh, E. & Grimes, R. (2007). PIV measurements of flow within plugs in a microchannel. *Microfluid Nanofluid*, Vol.3, pp. 463-472, ISSN 1613-4982.
- Koutsiaris, A.G.; Mathioulakis, D.S. & Tsangaris, S. (1999). Microscope PIV for velocity field measurement of particle suspensions flowing inside glass capillaries. *Meas. Sci. Technol.*, Vol.10, pp. 1037-1046, ISSN 0957-0233.
- Koutsiaris, A.G. (2005). Volume flow estimation in the precapillary mesenteric microvasculature *in-vivo* and the principle of constant pressure gradient. *Biorheology*, Vol.42, No 6, pp. 479-491, ISSN 0006-355X.
- Koutsiaris, A.G.; Tachmitzi, S.V.; Batis, N.; Kotoula, M.G., Karabatsas, C.H.; Tsironi, E. & Chatzoulis, D.Z. (2007). Volume flow and wall shear stress quantification in the human conjunctival capillaries and post-capillary venules *in-vivo*. *Biorheology*, Vol.44, No 5/6, pp. 375-386, ISSN 0006-355X.
- Koutsiaris, A.G. (2009). A velocity profile equation for blood flow in small arterioles and venules of small mammals *in vivo* and an evaluation based on literature data. *Clinical Hemorheology and Microcirculation*, Vol.43, No.4, pp. 321-334, ISSN 1386-0291.
- Koutsiaris, A.G.; Tachmitzi, S.V.; Kotoula, M.G. & Tsironi, E. (2010a). Old and new velocity profile equations of the blood flow *in vivo*: a preliminary evaluation. *Series on Biomechanics*, Vol.25, No 1-2, pp. 111-116, ISSN 1313-2458.
- Koutsiaris, A.G. (2010b). Velocity profile equations for microvessel blood flow in mammals. *Bulletin of the Portuguese Society of Hemorheology and Microcirculation*, Vol.25, No 1, pp. 5-1-, ISSN 0872-4938.
- Koutsiaris, A.G.; Tachmitzi, S.V.; Papavasileiou, P.; Batis, N.; Kotoula, M.G. & Tsironi, E. (2010c). Blood velocity pulse quantification in the human conjunctival pre-capillary arterioles. *Microvascular Research*, Vol.80, pp. 202-208, ISSN 0026-2862.
- Koutsiaris, A.G.; Tachmitzi, S.V. & Giannoukas, A.D. (2011). How good are the fittings of the velocity profiles *in vivo*? *3rd Micro and Nano Flows Conference*, Thessaloniki, Greece, 22-24 August, ISBN 978-1-902316-98-7, In press.

- Kuang, C.; Zhao, W.; Yang, F. & Wang, G. (2009). Measuring flow velocity distribution in microchannels using molecular tracers. *Microfluid Nanofluid*, Vol.7, pp.509-517, ISSN 1613-4982.
- Lee, S.J. & Kim, S. (2009). Advanced particle-based velocimetry techniques for Microscale flows. *Microfluid Nanofluid*, Vol.6, pp. 577-588, ISSN 1613-4982.
- Lima, R.; Wada, S.; Tsubota, K. & Yamaguchi T. (2006). Confocal micro-PIV measurements of three-dimensional profiles of cell suspension flow in a square microchannel. *Meas. Sci. Technol.*, Vol.17, pp. 797-808, ISSN 0957-0233.
- Lima, R.; Wada, S.; Takeda, M.; Tsubota, K. & Yamaguchi T. (2007). In vitro confocal micro-PIV measurements of blood flow in a square microchannel: The effect of the hematocrit on instantaneous velocity profiles. *Journal of Biomechanics*, Vol.40, pp. 2752-2757, ISSN 0021-9290.
- Lima, R.; Wada, S.; Tanaka, S.; Takeda, M.; Ishikawa, T.; Tsubota, K.; Imai, Y. & Yamaguchi T. (2008). In vitro blood flow in a rectangular PDMS microchannel: experimental observations using a confocal micro-PIV system. *Biomed Microdevices*, Vol.10, pp. 153-167, ISSN 1387-2176.
- Lima, R.; Ishikawa, T.; Imai, Y.; Takeda, M.; Wada, S. & Yamaguchi T. (2009). Measurement of individual red blood cell motions under high hematocrit conditions using a confocal micro-PTV system. *Annals of Biomedical Engineering*, Vol.37, pp. 1546-1559, ISSN 0090-6964.
- Lindken, R.; Westerweel, J. & Wieneke, B. (2006). Stereoscopic micro particle image velocimetry. *Exp Fluids*, Vol.41, pp. 161-171, ISSN 0723-4864.
- Lindken, R.; Rossi, M.; Große, S. & Westerweel, J. (2009). Micro-particle image velocimetry (PIV): recent developments, applications and guidelines. *Lab on a Chip – Miniaturisation for Chemistry and Biology*, Vol.9, No 17, pp. 2551-2567, ISSN 1473-0197.
- Lipowsky, H.H.; Usami, S. & Chien, S. (1980). *In vivo* measurements of " Apparent Viscosity" and microvessel hematocrit in the mesentery of the cat. *Microvascular Research*, Vol.19, pp. 297-319, ISSN 0026-2862.
- Long, D.S.; Smith, M.L.; Pries, A.R.; Ley, K. & Damiano, E.R. (2004). Microviscometry reveals reduced blood viscosity and altered shear rate and shear stress profiles in microvessels after hemodilution. *PNAS*, Vol.101(27), pp. 10060-10065, ISSN 0027-8424.
- Meinhart, C.D.; Wereley, S.T. & Santiago, J.G. (1999). Measurements of a microchannel flow. *Exp Fluids*, Vol.27, pp. 414-419, ISSN 0723-4864.
- Meinhart, C.D. & Zhang, H. (2000). The flow structure inside a microfabricated inkjet printhead. *Journal of Microelectromechanical Systems*, Vol.9, No 1, pp. 67-75, ISSN 1057-7157.
- Nabavi, M. (2009). Steady and unsteady flow analysis in microdiffusers and micropumps: a critical review. *Microfluid Nanofluid*, Vol.7, pp. 599-619, ISSN 1613-4982.
- Nakano, A.; Sugii, Y.; Minamiyama, M. & Niimi, H. (2003). Measurement of red cell velocity in microvessels using particle image velocimetry (PIV). *Clinical Hemorheology and Microcirculation*, Vol.29, No., pp. 445-455, ISSN 1386-0291.
- Nakano, A.; Sugii, Y.; Minamiyama, M.; Seki, J. & Niimi, H. (2005). Velocity profiles of pulsatile blood flow in arterioles with bifurcation and confluence in rat mesentery, *JSME International Journal Series C*, Vol.48, No. 4, pp. 444-452, ISSN 0914-8825.

- Nguyen, N.T. & Wereley, S.T. (2002). *Fundamentals and Applications of Microfluidics*, Artech House, ISBN 1-58053-343-4.
- Okuda, R.; Sugii, Y. & Okamoto, K. (2003). Velocity measurement of blood flow in a microtube using micro PIV system. Proceedings of PSFVIP-4, F4084, June 3-5, 2003, Chamonix, France.
- Olsen, M.G. & Adrian, R.J. (2000). Out of focus effects on particle image visibility and correlation in microscopic particle image velocimetry. *Exp. Fluids*, Suppl, pp. S166-S174, ISSN 0723-4864.
- Park, J.S.; Choi, C.K. & Kim, K.D. (2004). Optically sliced micro-PIV using confocal laser scanning microscopy (CSLM). *Exp. Fluids*, Vol.37, pp. 105-119, ISSN 0723-4864.
- Potter, D.R. & Damiano, E.R. (2008). The hydrodynamically relevant endothelial cell glycocalyx observed *in vivo* is absent *in vitro*. *Circ. Res.*, Vol.102, pp. 770-776, ISSN 0009-7330.
- Prasad, A.K.; Adrian, R.J.; Landreth, C.C. & Offutt, P.W. (1992). Effect of resolution on the speed and accuracy of particle image velocimetry interrogation. *Exp. Fluids*, Vol.13, pp. 105-116, ISSN 0723-4864.
- Raffel, M.; Wereley, S.T.; Willert, C.E. & Kompenhans, J. (2007). *Particle Image Velocimetry*, Springer, ISBN 3-540-72307-3, Heidelberg.
- Roelvros, J.M.J.G. (1974). Analogue processing of C.W.-Doppler flowmeter signals to determine average frequency shift momentarily without the use of a wave analyser, In: *Cardiovascular Applications of Ultrasound*, Reneman, R.S. (Ed.), pp. 43-54, ISBN 978 044 4106 31 5, Amsterdam-London.
- Santiago, J.G.; Wereley, S.T.; Meinhart, C.D.; Beebe, D.J. & Adrian, R.J. (1998). A particle image velocimetry system for micro fluidics. *Exp Fluids*, Vol.25, pp. 316-319, ISSN 0723-4864.
- Schmid-Schoenbein, G.W. & Zweifach, B.W. (1975). RBC velocity profiles in arterioles and venules of the rabbit omentum. *Microvascular Research*, Vol.10, pp. 153-164, ISSN 0026-2862.
- Sugii, Y.; Shigeru, N.; Okuno, T. & Okamoto, K. (2000). A highly accurate iterative PIV technique using a gradient method. *Meas. Sci. Technol.*, Vol.11, pp. 1666-1673, ISSN 0957-0233.
- Sugii, Y.; Shigeru, N. & Okamoto, K. (2002). *In vivo* PIV measurement of red blood cell velocity field in microvessels considering mesentery motion. *Physiol. Meas.*, Vol.23, pp. 403-416, ISSN 0967-3334.
- Tangelder, G.J.; Slaaf, D.W.; Muijtjens, A.M.M.; Arts, T.; Egbrink, M.G.A. & Reneman, R.S. (1986). Velocity profiles of blood platelets and red blood cells flowing in arterioles of the rabbit mesentery. *Circ. Res.*, Vol.59, pp. 505-514, ISSN 0009-7330.
- Thome, J.R. & Marcinichen, J.B. (2011). On-chip micro-evaporation: experimental evaluation of liquid pumping and vapour compression cooling systems. *3rd Micro and Nano Flows Conference*, Thessaloniki, Greece, 22-24 August, ISBN 978-1-902316-98-7, In press.
- Timgren, A.; Tragardh, G. & Tragardh, C. (2008). Application of the PIV technique to measurements around and inside a forming drop in a liquid-liquid system. *Exp Fluids*, Vol.44, pp. 565-575, ISSN 0723-4864.
- Tsukada, K.; Minamitani, H.; Sekizuka, E. & Oshio C. (2000). Image correlation method for measuring blood flow velocity in microcirculation: correlation "window"

- simulation and *in vivo* image analysis. *Physiol. Meas.*, Vol.21, pp. 459-471, ISSN 0967-3334.
- Vennemann, P.; Kiger, K.T.; Lindken, R.; Groenendijk, B.C.W.; Stekelenburg, S.; Hagen, T.L.M.; Ursem, N.T.C.; Poelmann, R.E.; Westerweel, J. & Hierck, B.P. (2006). In vivo micro particle image velocimetry measurements of blood-plasma in the embryonic avian heart. *Journal of Biomechanics*, Vol.39, pp. 1191-1200, ISSN 0021-9290.
- Werely, S.T. & Meinhart, C.D. (2001). Adaptive second-order accurate particle image velocimetry. *Exp Fluids*, Vol.31, pp. 258-268, ISSN 0723-4864.
- Werely, S.T. & Meinhart, C.D. (2005). Micron-Resolution Particle Image Velocimetry, In: *Microscale Diagnostic Techniques*, Breuer K.S. (Ed.), pp. 51-112, Springer, ISBN 3-540-23099-8, Heidelberg.
- Werely, S.T. & Meinhart, C.D. (2010). Recent Advances in Micro-Particle Image Velocimetry. *Annu. Rev. Fluid Mech.*, Vol.42, pp. 557-576, ISSN 0066-4189.
- Westerweel, J. (1997). Fundamentals of digital particle image velocimetry. *Meas. Sci. Technol.*, Vol.8, pp. 1379-1392, ISSN 0957-0233.
- Westerweel, J.; Geelhoed, P.F. & Lindken, R. (2004). Single-pixel resolution ensemble correlation for micro-PIV applications. *Exp. Fluids*, Vol.37, pp. 375-384, ISSN 0723-4864.
- Willert, C.E. & Gharib, M. (1991). Digital particle image velocimetry. *Exp. Fluids*, Vol.10, pp. 181-193, ISSN 0723-4864.
- Windberger, U.; Bartholovitsch, A.; Plasenzotti, R.; Korak, K.J. & Heinze, G. (2003). Whole blood viscosity, plasma viscosity and erythrocyte aggregation in nine mammalian species: reference values and comparison of data. *Experimental Physiology*, Vol.88, pp. 431-440, ISSN 0958-0670.
- Windberger, U. & Baskurt, O.K. (2007). Comparative Haemorheology, In: *Handbook of Hemorheology and Hemodynamics*, Baskurt, O.K.; Hardeman, M.R.; Rampling, M. & Meiselman, H.J. (Eds), pp. 267-283, IOS Press, ISBN 978-1-58603-771-0, The Netherlands.

IntechOpen



The Particle Image Velocimetry - Characteristics, Limits and Possible Applications

Edited by PhD. Giovanna Cavazzini

ISBN 978-953-51-0625-8

Hard cover, 386 pages

Publisher InTech

Published online 23, May, 2012

Published in print edition May, 2012

The Particle Image Velocimetry is undoubtedly one of the most important technique in Fluid-dynamics since it allows to obtain a direct and instantaneous visualization of the flow field in a non-intrusive way. This innovative technique spreads in a wide number of research fields, from aerodynamics to medicine, from biology to turbulence researches, from aerodynamics to combustion processes. The book is aimed at presenting the PIV technique and its wide range of possible applications so as to provide a reference for researchers who intended to exploit this innovative technique in their research fields. Several aspects and possible problems in the analysis of large- and micro-scale turbulent phenomena, two-phase flows and polymer melts, combustion processes and turbo-machinery flow fields, internal waves and river/ocean flows were considered.

How to reference

In order to correctly reference this scholarly work, feel free to copy and paste the following:

Aristotle G. Koutsiaris (2012). Digital Micro PIV (μ PIV) and Velocity Profiles In Vitro and In Vivo, The Particle Image Velocimetry - Characteristics, Limits and Possible Applications, PhD. Giovanna Cavazzini (Ed.), ISBN: 978-953-51-0625-8, InTech, Available from: <http://www.intechopen.com/books/the-particle-image-velocimetry-characteristics-limits-and-possible-applications/digital-micro-piv-piv-and-velocity-profiles-in-vitro-and-in-vivo>

INTECH
open science | open minds

InTech Europe

University Campus STeP Ri
Slavka Krautzeka 83/A
51000 Rijeka, Croatia
Phone: +385 (51) 770 447
Fax: +385 (51) 686 166
www.intechopen.com

InTech China

Unit 405, Office Block, Hotel Equatorial Shanghai
No.65, Yan An Road (West), Shanghai, 200040, China
中国上海市延安西路65号上海国际贵都大饭店办公楼405单元
Phone: +86-21-62489820
Fax: +86-21-62489821

© 2012 The Author(s). Licensee IntechOpen. This is an open access article distributed under the terms of the [Creative Commons Attribution 3.0 License](#), which permits unrestricted use, distribution, and reproduction in any medium, provided the original work is properly cited.

IntechOpen

IntechOpen